

# TURBULENCE IN PLANT CANOPIES

---

John Finnigan

*CSIRO Land and Water, F.C. Pye Laboratory, Canberra, Australia; e-mail:*

*john.finnigan@cbr.clw.csiro.au*

**Key Words** atmosphere, shear-flow, boundary-layer, vegetation, eddy

■ **Abstract** The single-point statistics of turbulence in the ‘roughness sub-layer’ occupied by the plant canopy and the air layer just above it differ significantly from those in the surface layer. The mean velocity profile is inflected, second moments are strongly inhomogeneous with height, skewnesses are large, and second-moment budgets are far from local equilibrium. Velocity moments scale with single length and time scales throughout the layer rather than depending on height. Large coherent structures control turbulence dynamics. Sweeps rather than ejections dominate eddy fluxes and a typical large eddy consists of a pair of counter-rotating streamwise vortices, the downdraft between the vortex pair generating the sweep. Comparison with the statistics and instability modes of the plane mixing layer shows that the latter rather than the boundary layer is the appropriate model for canopy flow and that the dominant large eddies are the result of an inviscid instability of the inflected mean velocity profile. Aerodynamic drag on the foliage is the cause both of the unstable inflected velocity profile and of a ‘spectral short cut’ mechanism that removes energy from large eddies and diverts it to fine scales, where it is rapidly dissipated, bypassing the inertial eddy-cascade. Total dissipation rates are very large in the canopy as a result of the fine-scale shear layers that develop around the foliage.

## 1. INTRODUCTION

It is almost twenty years since this subject appeared in Annual Reviews, with the excellent survey by Raupach & Thom (1981). Their review appeared at a turning point in the study of canopy flow. It presented some of the earliest results that showed unequivocally that turbulent flows in canopies are dominated by large coherent structures of whole canopy scale, results that challenged the earlier paradigm, where canopy turbulence was supposed to be a superposition of the energetic small-scale eddies produced in plant wakes onto standard surface-layer turbulence.

In the two decades since Raupach & Thom’s review a consistent view of the turbulent structure of canopy flows has emerged. Large coherent structures are an essential part of it, and we are now in a position to describe the mechanisms by which they arise, their phenomenology, and the way they are dissipated as they interact with the foliage, at least in the simplest cases of extensive uniform

canopies on level ground and in steady flow conditions. Nowadays the attention of workers is directed more and more to the practical realities of canopies on hills, behind windbreaks, near clearings or forest edges, or where the vegetation is sparse and irregular.

This corresponds in part with an upsurge of wider interest in canopy turbulence sparked by the need to understand global biogeochemical cycles and their role in climate change. This interest has led to a proliferation of continuous, long-term eddy-flux measurements of carbon dioxide and energy exchange between canopies and the atmosphere (Baldocchi & Meyers 1998). The need to measure eddy fluxes 24 hours a day, 365 days a year means that difficult conditions of non-stationarity, intermittency, and strong diabatic influences on the flow must now be confronted and understood.

It is the turbulent wind field that drives scalar exchange between vegetation and the atmosphere. Excursions into the difficult conditions that workers are now embracing are best made from a base of firm understanding of canopy turbulence dynamics in simpler situations. This thought defines the scope of this review. Rather than survey the many different inhomogeneous and non-stationary experiments now being reported, we attempt to present a consistent picture of flow dynamics in simple canopies, the fruit of the last twenty years. Pointers to more complex situations are left to the conclusions.

The paper is organized in the following way. In §2 we present the analysis framework and flow equations used in later sections and in canopy studies generally. In §3 we survey turbulent statistics in the canopy layer, contrasting them with the more familiar surface layer above. §4 is devoted to describing the large coherent structures that dominate turbulence in the canopy and give it its special character. Their elucidation could be said to have defined the main agenda of canopy studies since Raupach & Thom's (1981) review. In §5 we propose an heuristic model for these structures that unifies much of what is observed and suggests scaling laws for canopy flow. Sections 3, 4, and 5 follow very closely the development in Raupach et al (1996) albeit with different emphases; the present author is indebted to his colleagues Dr. MR Raupach and Dr. Y Brunet for the use of this material. In §6 attention focuses on the fine structure of canopy turbulence as revealed by velocity spectra and a new theory of the spectral shape is presented. Finally, in §7, the large and fine scales are brought together by considering the turbulent kinetic energy budget and the generation and dissipation of canopy turbulence.

## 2. THE ANALYSIS FRAMEWORK

It is impractical to account explicitly for the spatial variability imposed on the airflow by the complexity of the within-canopy airspace. Instead, for many years standard free-air Reynolds equations were adapted for use in canopies by the ad-hoc addition of a source or drag term, which was regarded as a smooth function

of space. When attempts to write second-order closure models of canopy flow were made, however, the limitations of this approach quickly became apparent. At second order the drag term appeared as a strong non-Newtonian viscous damping of the turbulence, augmenting regular viscous dissipation and some orders of magnitude larger. In reality, as was well known, the interaction of the wind field with the foliage ought to produce large amounts of fine-scale turbulence in the wakes of canopy elements.

The paradox was resolved when Wilson & Shaw (1977) showed that a rigorous spatial averaging procedure, when applied to the moment equations that obtain at a point in the canopy airspace, produced equations for the area-averaged wind field containing the required smooth source and drag terms as well as terms corresponding to the production of fine-scale 'wake turbulence'. The equations also contained extra 'dispersive flux' terms that had not been formally included in analyses up to that point and which were the spatial analogues of the Reynolds stresses that attend time averaging. The spatial averages used by Wilson & Shaw (1977) and further developed by Raupach & Shaw (1982) were averages over a horizontal plane. The more general volume average was subsequently introduced by Finnigan (1985) and Raupach et al (1986). We discuss these concepts next.

In this paper we use a right-handed rectangular Cartesian coordinate system,  $x_i (x, y, z)$  with  $x_1 (x)$  aligned with the mean velocity and  $x_3 (z)$  normal to the ground surface. Velocity components are denoted by  $u_i$ , ( $u, v, w$ ) with  $u_1 (u)$  the streamwise and  $u_3 (w)$  the vertical component. When it is more convenient, vector quantities may also be indicated by bold type, viz.  $x_i \equiv \mathbf{x}$ . When we employ tensor notation we adopt the convention that repeated Latin indices are to be summed over, e.g.,  $u_i u_i = u_1^2 + u_2^2 + u_3^2$ , while repeated Greek indices are not summed,  $u_\alpha u_\alpha = u_\alpha^2$ .

The time average operator is denoted by an overbar:

$$\bar{a}(t) = \frac{1}{T} \int_{t-T/2}^{t+T/2} a(t') dt', \quad (2.1)$$

and fluctuations about the time mean by a prime so

$$u_i = \bar{u}_i + u'_i \quad \text{where,} \quad \overline{u'_i} = 0. \quad (2.2)$$

The volume average of a scalar or vector function  $\phi_j$  is defined as:

$$\langle \phi_j \rangle(\mathbf{x}, t) = \frac{1}{V} \iiint_V \phi_j(\mathbf{x} + \mathbf{r}, t) d^3 \mathbf{r}, \quad (2.3)$$

where the averaging volume  $V$ , which excludes solid plant parts, consists of a horizontal slab, extensive enough in the horizontal to eliminate plant-to-plant variations in canopy structure but thin enough to preserve the characteristic variation of properties in the vertical.

All flow variables may be decomposed into their volume average and a departure therefrom:

$$\phi_j = \langle \phi_j \rangle + \phi_j'', \quad (2.4)$$

where the departure satisfies:

$$\langle \phi_j''(x, t) \rangle = 0. \quad (2.5)$$

In the multiply-connected canopy airspace, differentiation and volume averaging do not commute for variables that are not constant at air-canopy interfaces. This is true in all cases for spatial differentiation and also for differentiation with respect to time in the case of a waving canopy. Instead it can be shown (Finnigan 1985, Raupach et al 1986) that:

$$\begin{aligned} \left\langle \frac{\partial \phi_j}{\partial x_i} \right\rangle &= \frac{\partial \langle \phi_j \rangle}{\partial x_i} - \frac{1}{V} \iint_{S_i} \phi_j n_i dS, \\ \left\langle \frac{\partial \phi_j}{\partial t} \right\rangle &= \frac{\partial \langle \phi_j \rangle}{\partial t} - \frac{1}{V} \iint_{S_i} \phi_j v_i n_i dS, \end{aligned} \quad (2.6)$$

where the surface  $S_i$  is the sum of all the solid plant surfaces that intersect the averaging volume  $V$ ,  $n_i$  is the unit normal vector pointing away from  $S_i$  into  $V$ , and  $v_i$  is the velocity of a point on the plant surface.

To derive the rate equation for a given velocity moment in the canopy, we begin with the Reynolds equation that obtains at a point in the canopy airspace, decompose each of its terms into volume averages and departures therefrom, then apply the volume averaging operator (2.3) and the identities (2.6). The resulting first-moment or momentum equation for adiabatic flow is

$$\frac{\partial \langle \bar{u}_i \rangle}{\partial t} + \langle \bar{u}_j \rangle \frac{\partial \langle \bar{u}_i \rangle}{\partial x_j} = - \frac{\partial \langle \bar{p} \rangle}{\partial x_i} + \frac{\partial \tau_{ij}}{\partial x_j} + f_{Fi} + f_{vi} \quad (2.7)$$

where

$$\tau_{ij} = - \langle \bar{u}_i' \bar{u}_j' \rangle - \langle \bar{u}_i'' \bar{u}_j'' \rangle + \nu \frac{\partial \langle \bar{u}_i \rangle}{\partial x_j} \quad (2.8)$$

$$f_{Fi} = \frac{1}{V} \iint_{S_i} \bar{p} n_i dS \quad (2.9)$$

$$f_{vi} = - \frac{\nu}{V} \iint_{S_i} \frac{\partial \bar{u}_i}{\partial n} dS. \quad (2.10)$$

In these equations  $p$  is the kinematic pressure and  $\nu$  the kinematic viscosity. The volume averaged kinematic momentum flux tensor  $\tau_{ij}$  includes the conventional turbulent and viscous stresses as well as the dispersive flux term, the second term on the RHS of (2.8), which results from any spatial correlations in the time-averaged velocity field. The presence of terms  $f_{Fi}$  and  $f_{vi}$  is a direct consequence of the non-commutivity of differentiation and volume averaging in the multiply-connected canopy airspace.  $f_{Fi}$  is (minus) the sum of the form or pressure drag

forces and  $f_{vi}$  is (minus) the sum of the viscous drag forces exerted on every surface element that intersects the averaging volume  $V$ . Together they constitute the aerodynamic drag on unit mass of air within  $V$ .

The time-averaging and volume-averaging operators (2.1) and (2.3) do not obey Reynolds averaging rules except in the limits of infinite averaging time ( $T \rightarrow \infty$ ) and  $V$  becoming an infinite horizontal slab of vanishing thickness. In the former circumstance, the time derivative of the moments would also vanish. When  $T$  and  $V$  are not infinite, the stress tensor  $\tau_{ij}$  contains extra ‘‘Leonard stress’’ terms augmenting both  $\langle \overline{u_i'' u_j''} \rangle$  and  $\langle \overline{u_i' u_j'} \rangle$  (Leonard 1974, Finnigan 1985). As a practical compromise we assume that the time-averaging period  $T$  and the horizontal extent of  $V$  are sufficiently large and  $V$  thin enough that these extra terms can be ignored, while we have retained the leading time derivative term to represent variations of the mean moments on time scales longer than  $T$ . We thereby retain correspondence with textbook equations that are generally derived using the mathematically convenient but experimentally unattainable ensemble average.

The same procedures can be applied to the second moment equations giving the following result for the general, volume-averaged stress budget in adiabatic flow,

$$\begin{aligned}
 & \left( \frac{\partial}{\partial t} + \langle \overline{u_j} \rangle \frac{\partial}{\partial x_j} \right) \langle \overline{u_i' u_k'} \rangle = - \left( \langle \overline{u_j' u_k'} \rangle \frac{\partial \langle \overline{u_i} \rangle}{\partial x_j} + \langle \overline{u_i' u_j'} \rangle \frac{\partial \langle \overline{u_k} \rangle}{\partial x_j} \right) \\
 & \quad - \frac{\partial \langle \overline{u_j'' u_i'' u_k''} \rangle}{\partial x_j} - \left( \langle \overline{u_j' u_k''} \rangle \frac{\partial \overline{u_i''}}{\partial x_j} + \langle \overline{u_i' u_j''} \rangle \frac{\partial \overline{u_k''}}{\partial x_j} \right) \\
 & \quad - \frac{\partial \langle \overline{u_i' u_j' u_k'} \rangle}{\partial x_j} - \left( \frac{\partial \langle \overline{p' u_i'} \rangle}{\partial x_k} + \frac{\partial \langle \overline{p' u_k'} \rangle}{\partial x_i} \right) + \text{v} \frac{\partial^2 \langle \overline{u_i' u_k'} \rangle}{\partial x_j \partial x_j} \\
 & \quad + \left\langle \overline{p' \left( \frac{\partial u_i'}{\partial x_k} + \frac{\partial u_k'}{\partial x_i} \right)} \right\rangle - 2\text{v} \left\langle \overline{\frac{\partial u_i'}{\partial x_j} \frac{\partial u_k'}{\partial x_j}} \right\rangle + \\
 & \quad \frac{1}{V} \left[ \int \int_{S_t} \overline{p' (v_i' n_k + v_k' n_i)} dS - \text{v} \int \int_{S_t} \left( v_k' \frac{\partial u_i'}{\partial n} + v_i' \frac{\partial u_k'}{\partial n} \right) dS \right]. \quad (2.11)
 \end{aligned}$$

X

Compared to ‘free-air’ second moment equations, there are three novel features of (2.11). First, as in (2.10), moments that would simply be time averages in free-air equations are now time and volume averages. Second, a set of terms have

appeared that represent spatially averaged correlations between the local variations of properties around the spatial mean. These terms can have important physical meaning. Focusing on term IV and comparing it with the shear production term, II, we see that IV represents the spatial average of the work done against local variations in the Reynolds stresses by local variations in the rates of strain. These local departures in stresses and strains are associated with the wakes and boundary layers of individual plant elements and it is this term, usually called ‘wake production’, that accounts for the fine-scale turbulence produced as the mean flow does work against the pressure drag of the foliage (Raupach & Shaw 1982). In similar fashion, the ‘dispersive’ transport term III is analogous to V and represents any net movement of stress caused by spatial correlations between local variations of stress and mean velocity.

Third, also as in Equation (2.10), surface integral terms like X have appeared as a result of the non-commutivity of the spatial averaging operator. The first part of X represents the correlation between plant motion and pressure drag on the plant parts, while the second part is the plant motion-viscous drag correlation. In coherently waving canopies like cereal crops the first of these can produce large instantaneous excursions in the covariance but in most circumstances we expect their time-averaged contributions to be small (Finnigan 1979, Shaw et al 1983). A more detailed discussion of the derivation of these equations and their properties can be found in Raupach & Shaw (1982), Finnigan (1985) and Brunet et al (1994).

The application of the volume average operator has removed the dependence of the flow equations on the stochastic distribution of the foliage. Unfortunately, we rarely, if ever, measure the volume-averaged variables that appear in the canopy equations! Practical considerations dictate that sensors be placed in the open spaces between the foliage and, because the boundary layers on clumped foliage will ensure that velocities are lower in regions of the canopy where we cannot measure, we must always consider the possibility of systematic biases in our measurements (see §6.1). While there is some evidence that in open uniform canopies the energetic mixing engendered by the high levels of turbulence will smooth out much of the systematic spatial differences in time-averaged velocity, so that dispersive fluxes like  $\langle \overline{u_i'' u_j''} \rangle$  are only a few percent of  $\langle \overline{u_i' u_j'} \rangle$  (Raupach et al 1986), other recent wind tunnel results in a model orchard suggest that the dispersive momentum flux can be of a magnitude similar to  $\langle \overline{u_i' u_j'} \rangle$  in the lower canopy (M Bohm, personal communication).

### 3. CHARACTERISTICS OF CANOPY TURBULENCE

#### 3.1. Velocity Moments

In Figure 1a-i we present a set of ‘family portraits’ of single-point turbulence statistics measured in near-neutral flow in twelve horizontally homogeneous canopies, ranging from wind tunnel models through cereal crops to forests. Canopy

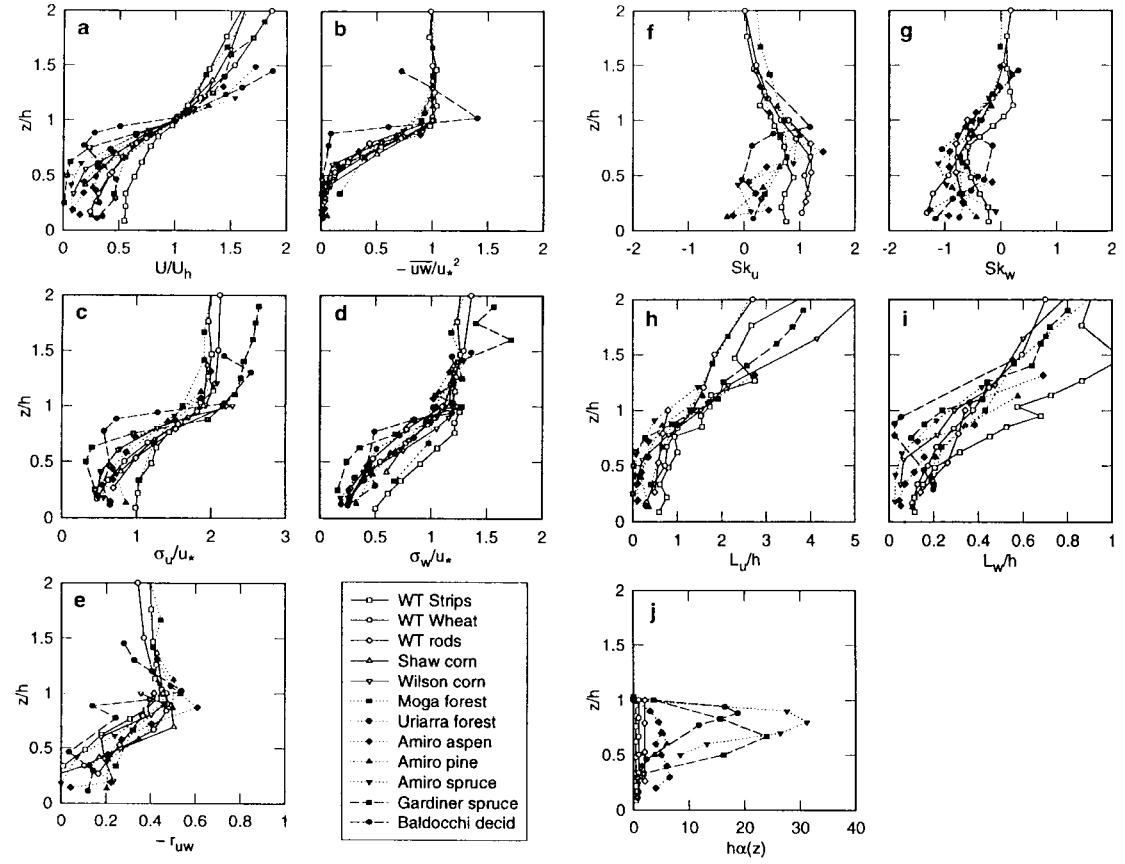


**Figure 1** (a–e) A “family portrait” of canopy turbulence for canopies A to L in Table (1), showing profiles with normalized height  $z/h$  of (a)  $U/U_h = \langle \overline{u_1} \rangle(z) / \langle \overline{u_1} \rangle(h)$ ; (b)  $-u'w'/u_*^2$ ; (c)  $\sigma_u/u_*$ ; (d)  $\sigma_w/u_*$ ; (e)  $-r_{uw} = -\overline{u'w'}/\sigma_u\sigma_w$ ; (f)  $Sk_u$ ; (g)  $Sk_w$ ; (h)  $L_u$ ; (i)  $L_w$ ; (j)  $h\alpha(z)$  where  $\alpha(z)$  is leaf area per unit volume.  $L_u$  and  $L_w$  are defined in equation (3.1). Figure from Raupach et al (1996)

data were first compared in this way by Raupach (1988), and the present data set is taken from Raupach et al (1996). The canopies span a wide range of roughness density  $\lambda$  (defined as the total frontal area of canopy elements per unit ground area) and a 500-fold height range. The vertical axis and length scales are normalized with canopy height  $h$  and velocity moments with either  $U_h = \bar{u}(h)$  or the friction velocity,  $u^* = \sqrt{-\overline{u'w'}}$ , where  $u^*$  is measured in the constant stress layer above the canopy. Details for each experiment are given in Table 1. The observations in Figure 1 have many common features, their differences being mainly attributable to their differing foliage area distribution. Figure 1j shows that the main differences in this parameter lie in the extent to which the foliage is clustered in a crown at the canopy top.

The normalized mean velocity profiles  $\bar{u}(z)/U_h$  shown in Figure 1a all have a characteristic inflection point at  $z = h$ . The shear is maximal at  $z = h$ , and its strength can be described by the length scale  $L_h = \bar{u}(h)/(\partial\bar{u}(h)/\partial z)$ . Above the canopy we observe a standard boundary layer profile, whereas within the canopy space the profile can be described as roughly exponential. As we shall see later, it is now believed that the inflexion point plays a critical role in canopy dynamics.

In Figure 1b, the momentum flux normalized by  $u^*$ , we see a standard constant stress layer above the canopy and then the rapid decay of  $-\overline{u'w'}$  as streamwise momentum is absorbed as aerodynamic drag on the foliage. Note that in all cases  $-\overline{u'w'}$  is practically zero by ground level, indicating that all of the horizontal momentum has been absorbed by the canopy elements even though some of the canopies in the ensemble are not particularly dense. The standard deviations of streamwise and vertical fluctuations, pictured in Figures 1c and d, are more scat-

**TABLE 1** Physical and aerodynamic parameters of the canopies in Figure 1. The roughness density or frontal area index  $\lambda$  is assumed to be half the single-sided leaf area index for field canopies.

Canopy	Identifier	h(m)	$\lambda$	$Uh/u^*$	$Ls/h$	Reference
WT strips	A	0.06	0.23	3.3	0.85	Raupach et al (1986)
WT wheat	B	0.047	0.47	3.6	0.57	Brunet et al (1994)
WT rods	C	0.19	1	5.0	0.49	Seginer et al (1976)
Shaw Corn	D	2.6	1.5	3.6	0.39	Shaw et al (1974)
Wilson Corn	E	2.25	1.45	3.2	0.46	Wilson et al (1982)
Moga eucalypt	F	12	0.5	2.9	0.58	Unpublished
Uriarra pine	G	20	2.05	2.5	0.29	Denmead & Bradley (1987)
Amiro Aspen	H	10	1.95	2.6	0.58	Amiro (1990)
Amiro pine	I	15	1	2.2	0.50	Amiro (1990)
Amiro spruce	J	12	5	2.4	0.44	Amiro (1990)
Gardiner spruce	K	12	5.1	4.0	0.30	Gardiner (1994)
Baldocchi deciduous	L	24	2.5	2.8	0.12	Baldocchi & Meyers (1988a,b)



tered than  $-\overline{u'w'}$  within the canopy but are also strongly inhomogeneous.  $\sigma_u/u^*$  values seem to group around 0.75 in the lower canopy, indicating that there is a good deal of horizontal ‘sloshing’ motion there but that this motion is *inactive* in the sense that it is not associated with much momentum transport.

Figure 1e, the correlation coefficient  $r_{uw} = \overline{u'w'}/\sigma_u\sigma_w$ , can be interpreted as the efficiency of momentum transport. Well above the canopy,  $r_{uw}$  assumes its standard surface layer value of about 0.32, corresponding to  $\sigma_u/u^* = 2.5$ ,  $\sigma_w/u^* = 1.25$ , values typical of a constant stress surface layer (Garratt 1992). At the canopy top in contrast, the stress ratios fall to  $\sigma_u/u^* = 2.0$ ,  $\sigma_w/u^* = 1.0$ , producing a value of  $r_{uw} = -0.5$ . Although there is a good deal of scatter in the data, it is clear that the turbulence around the canopy top transports substantially more momentum per unit variance than in the surface layer above.

Moving from second to third moments we observe in Figures 1f and g that the skewnesses of streamwise and vertical velocity fluctuations are of order +1 and -1, respectively, in the canopy space, in sharp contrast to the near-zero values these statistics assume in the surface layer.

### 3.2 Length and Time Scales

In Figures 1h and 1i we plot the streamwise  $L_u$  and vertical  $L_w$  Eulerian integral length scales obtained from integral time scales using Taylor’s hypothesis,

$$L_u = \frac{\bar{u}}{\sigma_u^2} \int_0^\infty \overline{u'_1(t)u'_1(t + \tau)} d\tau; \quad L_w = \frac{\bar{u}}{\sigma_w^2} \int_0^\infty \overline{u'_3(t)u'_3(t + \tau)} d\tau. \quad (3.1)$$

Both these scales are much larger than the size of individual canopy elements, reaching  $L_u \cong h$ ;  $L_w \cong h/3$  in the upper canopy.

An alternative way of obtaining turbulent time scales is through frequency spectra, which have been measured on many occasions in canopies. We discuss spectra in detail in section 6 but here we note that  $f p_\alpha$ , the location of the spectral peak on a plot of  $f S_\alpha(f)$  versus  $\ln(f)$ , where  $f$  is frequency and  $S_\alpha(f)$  is power spectral density, has quite different behavior within the canopy and in the surface layer above. In near neutral conditions in the surface layer  $f_{p\alpha}$  is proportional to  $(z - d)/\bar{u}(z)$  in accordance with surface layer similarity theory, where  $d$  is the displacement height of the logarithmic profile well above the canopy, whereas within and just above the canopy, measurements of  $f_{p\alpha}$  satisfy  $f_{pu} h/\bar{u}(h) \cong 0.15 \pm 0.05$  for the  $Su(f)$  spectrum and  $f_{pw} h/\bar{u}(h) \cong 0.45 \pm 0.05$  for the  $Sw(f)$  spectrum (Kaimal & Finnigan 1994).

### 3.3 Second Moment Budgets

The turbulent kinetic energy (TKE) budget is discussed in detail in section 7. Here we refer forward to Figure 17 and observe that the budget changes from a local-equilibrium form in the surface layer well above the canopy, where shear production and viscous dissipation are closely balanced, to a state where turbulent

and pressure transport terms are of the same order as the production terms within the canopy. This non-local state, with much of the TKE in the lower canopy imported from regions of high production around the canopy top, is observed to a greater or lesser degree in all canopy second moment budgets, both variance and covariance.

### 3.4 Eddy Diffusivities

The eddy diffusivities for momentum and heat are useful diagnostic properties of the flow. They are defined as

$$K_M = \frac{-\overline{u'w'}}{\partial \bar{u}/\partial z}; K_H = \frac{-\overline{w'\theta'}}{\partial \bar{\Theta}/\partial z}, \quad (3.2)$$

where  $\bar{\Theta}$  and  $\theta'$  denote mean and fluctuating potential temperatures, respectively. In the surface layer well above the canopy, their values are given by Monin-Obukhov similarity theory ( $K_M = K_H = \kappa_v u^*(z - d)$  in neutral conditions, where  $\kappa_v$  is von Karman's constant). In the region just above the canopy ( $h < z \leq 3h$ ),  $K_M$  and  $K_H$  are enhanced above their surface layer values. The degree of enhancement increases with proximity to the canopy top and also varies with canopy morphology. In neutral conditions, just above  $z = h$ ,  $K_M$  is increased by a factor between 1.1 and 1.5, while  $K_H$  increases by a factor of 2 to 3 (for more information and references see Kaimal & Finnigan 1994 and Raupach et al 1996). Hence the turbulent Prandtl number,  $K_M/K_H$ , decreases from a value close to 1.0 in the surface layer to about 0.5 at the top of the canopy.

Descending into the canopy, observations of  $K_M$  and  $K_H$  no longer show simple patterns and often become zero or negative. In such regions of counter-gradient diffusion, there is no longer a local relationship between the flux and the gradient, and the eddy diffusivity is not a useful description of turbulent transport (Shaw 1977, Denmead & Bradley 1985, 1987). Figure 2 from Denmead & Bradley (1985) shows three examples of counter (or zero) gradient steady diffusion of scalars in a uniform pine forest. Explanations for this behavior within the canopy can be advanced in an Eulerian (Finnigan 1985, Finnigan & Raupach 1987) and a Lagrangian framework (Raupach 1988), the latter providing a practical and physically correct alternative to eddy diffusivity models for turbulent transport of scalars. Both explanations rely in an essential way on observations showing that the eddies effecting turbulent transport in and just above the canopy are intermittent coherent structures of whole canopy scale, evidence that we review in the next section.

The distinctive character of the turbulence statistics in this region extending from the ground up to two or three canopy heights has earned it a name, the roughness sublayer to distinguish it from the surface layer above (Raupach et al 1991). In the following sections we also find it convenient to distinguish the layer actually occupied by vegetation, the 'canopy layer' from the roughness sublayer as a whole.

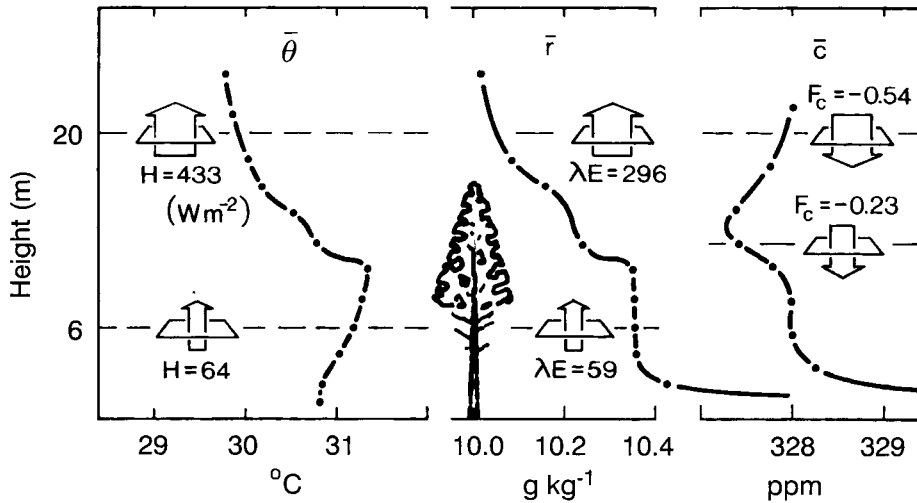


**Figure 2** Simultaneous fluxes and gradients of heat and temperature, latent heat and water vapor mixing ratio and carbon dioxide ( $\text{gm m}^{-2}\text{s}^{-1}$ ) and ppm. Obtained in a pine forest (Canopy G of Table 1). Figure from Denmead & Bradley (1987).

#### 4. COHERENT EDDIES IN CANOPIES

From the mid-1960s to the late 1970s our appreciation of the structure of turbulent flows was revolutionized. New methods of flow visualisation and signal processing revealed that the energy-containing motion in free shear layers and boundary layers was organized into distinct, coherent structures (Cantwell 1981, Robinson 1991). Beginning in the mid-1970s the same techniques were applied to canopies, and the roughness sublayer also was found to be populated by distinct coherent eddies that were responsible for much of its unique character.

##### 4.1 Two-Point Turbulence Statistics

As in the free boundary layer, the notion that the dominant turbulent motion in canopies was of large scale had been foreshadowed by early measurements of spectra and two-point covariances (Allen 1968). Since then steadily more sophisticated statistical approaches have continued to provide information on integral scales. Single-point and multi-point measurements in wind tunnels (e.g., Seginer & Mulhearn 1978, Raupach et al 1986, Shaw et al 1995), crops (e.g., Finnigan 1979, Shaw et al 1974), and forests (e.g., Baldocchi & Meyers 1988a, Amiro 1990, Gardiner 1994) have painted a consistent picture of horizontal Eulerian integral length scales of order  $h$  while vertical Eulerian scales cluster about  $h/3$ , as we have already shown in Figure 1h,i.

To derive spatial information on the structure of turbulence from single-point statistics, however, we need to assume Taylor's frozen turbulence hypothesis—always a questionable assumption in high-intensity canopy turbulence. To access the spatial structure directly we must resort to multi-point measurements. In a horizontally homogeneous stationary flow, the two-point space-time correlation tensor is defined as

$$r_{ij}(x, y, z, \tau; z') = \frac{\overline{u_i(x, y, z, t + \tau) u_j(0, 0, z', t)}}{(\overline{u_i^2(z)})^{1/2} (\overline{u_j^2(z')})^{1/2}}, \quad (4.1)$$

where the reference sensor is placed at the origin of horizontal coordinates  $(0, 0, z')$ . Measurements of  $r_{ij}$  generally fall into two groups:  $r_{ij}(x, y, z; z')$  usually obtained in wind tunnels and  $r_{ij}(0, 0, z, \tau; z')$  obtained from two or more probes on a single tower.

The most complete set of observations of the spatial correlation with zero time delay,  $r_{ij}(x, y, z; z')$  comes from the wind tunnel experiment of Shaw et al (1995). Figure 3a displays contours of  $r_{11}(x, 0, z; h)$ , the projection on the  $(x, 0, z)$  plane of the  $u - u$  correlation with the reference sensor at  $z = h$ . We observe a tilted elongated elliptical region of strong correlation ( $|r_{11}| > 0.2$ ) extending roughly  $10h$  in the streamwise direction and  $4h$  in the vertical. The tilt angle of the major axis of the ellipse is about 20 degrees relative to the wall. In Figure 3b we see  $r_{11}(0, y, z; h)$ , the projection of the same  $u - u$  correlation onto the  $(0, y, z)$  plane. Now we observe a concentrated region of strong correlation around  $y = 0$  with symmetrical negative lobes on either side. The lateral and vertical extents of the region of strong correlation are similar to those deduced from Figure 3a, roughly  $10h$  and  $4h$ , respectively.

The vertical velocity is well correlated over a much more restricted region. Contours of  $r_{33}(x, 0, z; h)$  in the  $(x, 0, z)$  plane (Figure 3c) are roughly circular with a diameter of about  $2h$ , while in the  $(0, y, z)$  plane (Figure 3d) contours of  $r_{33}(0, y, z; h)$  form vertically elongated ovoids confined within  $y/h \cong \pm 0.5$ .

These differences in the behavior of streamwise and vertical two-point, zero time-delay correlations are also reflected in vertically separated time-delayed correlations,  $r_{ij}(0, 0, z, \tau; z')$ . Data from single towers in the field or from model canopies show a consistent pattern in streamwise  $r_{11}(0, 0, z, \tau; z')$  and vertical  $r_{33}(0, 0, z, \tau; z')$  correlations (Finnigan 1979, Baldocchi & Meyers 1988a, Gao et al 1989, Raupach et al 1989, Shaw & Zhang 1992). With the reference sensor at  $z'$  fixed high above the canopy, the peak of maximum correlation moves to successively longer time delays as the moving sensor descends into the upper canopy. This behavior is consistent with the streamwise advection of a series of eddies tilted in the sense of the  $u - u$  contours shown in Figure 3a. When the moving sensor reaches the lower canopy, however, this pattern reverses; the peak of maximum correlation occurs at shorter time delays and may eventually lead to the arrival of the signal at higher levels (Shaw & Zhang 1992, Raupach et al 1989).

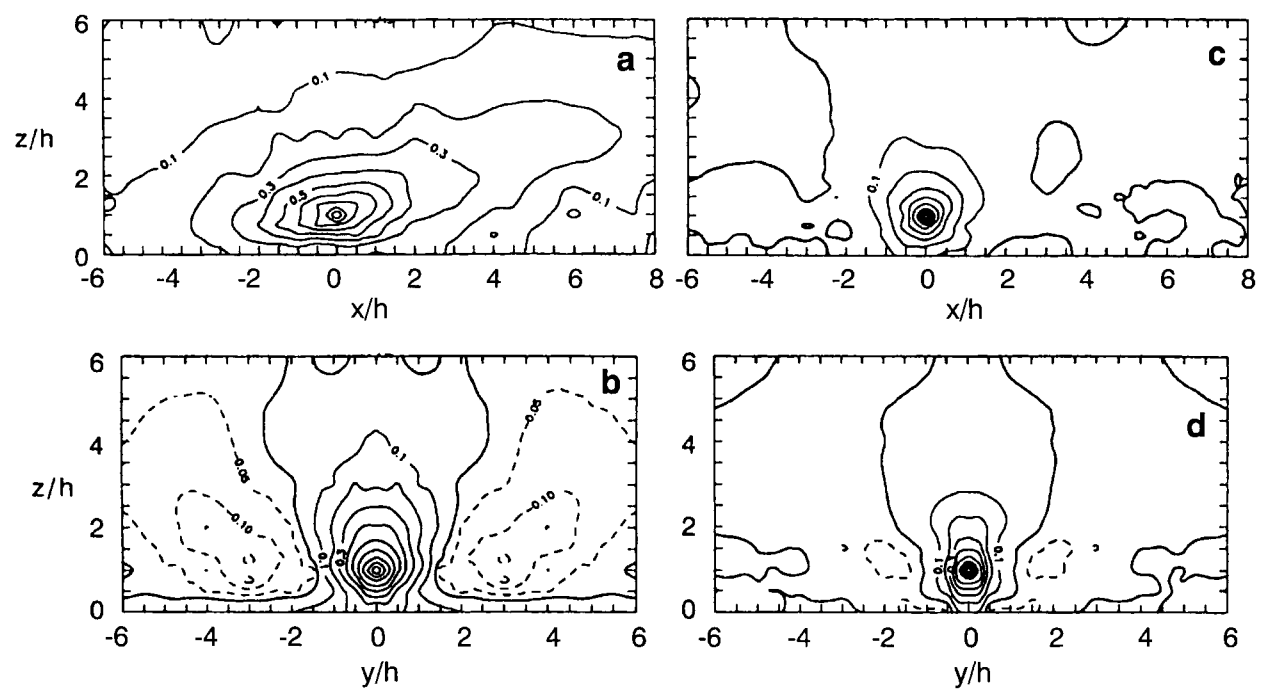


**Figure 3** Contours of the two-point, one-time velocity correlation function (a)  $r_{11}(x,0,z;h)$  on the  $(x,0,z)$  plane; (b)  $r_{11}(0,y,z;h)$  on the  $(0,y,z)$  plane; (c)  $r_{33}(x,0,z;h)$  on the  $(x,0,z)$  plane; (d)  $r_{33}(0,y,z;h)$  on the  $(0,y,z)$  plane. Data from Shaw et al (1995).

In contrast, the peak of the vertical correlation  $r_{33}(0,0,z,\tau;z')$  exhibits no time delay with increasing separation of reference and moving probe. The signal apparently arrives at the same time at all heights. At the moment these results await a complete explanation, although Shaw & Zhang (1992) have shown they are consistent with the fact that  $u'$  fluctuations are forced both by  $\partial p'/\partial x$  and  $w'\partial\langle\bar{u}\rangle/\partial z$ , while  $\partial p'/\partial z$  alone forces  $w'$ . The results remind us that coherent structures in canopy flows, just as in other shear flows, are complex patterns of pressure, velocity, and translating air particles and that their presence is manifested in different ways depending upon which variables we choose to measure.

Two-point correlation data also allow us to compute integral length scales and convection velocities directly without recourse to Taylor's hypothesis. Shaw et al (1995) integrated the zero time delay correlation function  $r_{ij}(x,y,z;z')$  along a streamwise transect to compute streamwise ( $L_1 = L_u$ ) and vertical ( $L_3 = L_w$ ) scales in a wind tunnel model wheat canopy,

$$L_\alpha^{\cdot\cdot}(z) = \int_0^\infty r_{\alpha\alpha}(x,0,z,0;z')dx \quad (4.2)$$

where the  $\cdot\cdot$  indicates a two-point integral scale. In Figure 4a these are compared with the corresponding single-point integral scales obtained by Equation 3.1. Within the canopy the two-point scales are both larger by about a factor of two and vary much more slowly with height, changing less than 30% across the roughness sublayer. A major reason for this discrepancy is that the mean velocity

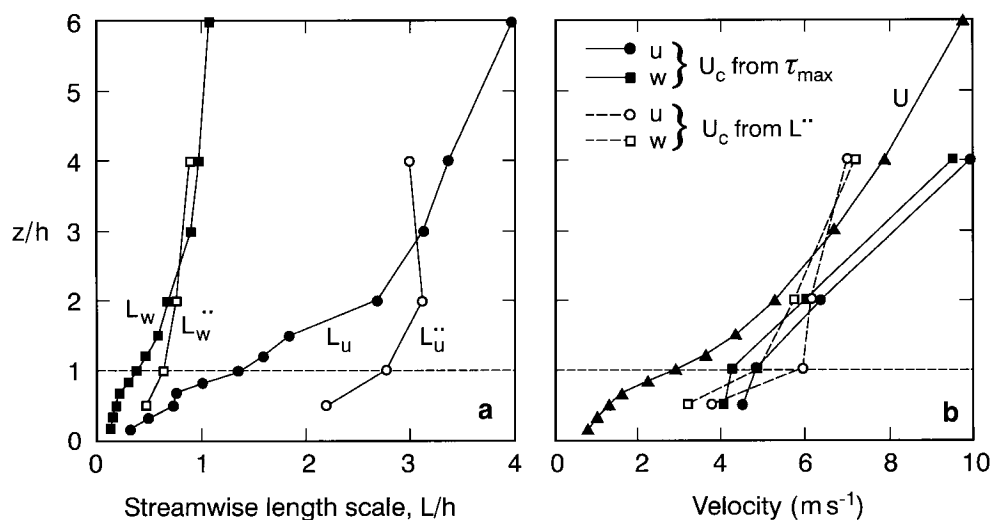


**Figure 4** Comparison of: (a) two-point  $L_u^{\cdot\cdot}$ ,  $L_w^{\cdot\cdot}$  and single-point  $L_u$ ,  $L_w$  integral length scales in a model wheat canopy; (b) mean velocity  $U = \langle \bar{u}_1 \rangle$  and large eddy convection velocity in a model wheat canopy. Figure from Shaw et al (1995).

is a poor estimate of the convection velocity of the eddies that dominate the correlation fields.

Shaw et al (1995) computed the convection velocity  $U_c$  from two-point data, using two different approaches: first as  $U_c = x/\tau_{\max}$ , where  $\tau_{\max}$  is the time delay of the peak in  $r_{11}(x, 0, z, \tau; z)$ , and second, using the ratio of single to two-point length scales, viz.  $U_c = \bar{u}(z)L_\alpha/L_\alpha$ . Both estimates are compared with  $\bar{u}(z)$  in Figure 4b and give values of  $U_c$  within the canopy that are much larger than the mean velocity,  $U_c(z)/\bar{u}(z)$ , being approximately 2 just above  $z = h$ . Just as in the case of the integral scales, the convection velocity varies much less than the mean velocity through the roughness sublayer.

## 4.2 Conditional Analysis

*Conditional analysis* or *conditional sampling* describes a broad class of methods where sampling of the data series is triggered by the occurrence of a particular pattern in the data, the pattern being chosen to correspond to some preconception about the space or time structure of the coherent eddy (Antonia 1981).

The quadrant-hole technique (Q-H) (Lu & Willmarth 1973) was first applied to a wheat crop by Finnigan (1979) and has since been used to investigate a wide range of canopies including wind tunnel models (e.g., Raupach et al 1986), cereal canopies (e.g., Shaw et al 1983), and forests (e.g., Baldocchi & Meyers 1988b, Gardiner 1994). Taking the Reynolds shear stress,  $\overline{u'w'}$  as an example, the quadrant hole technique involves integrating the joint probability density function (pdf) of  $u'$  and  $w'$  over quadrants defined by the four sign combinations, viz:

- Quadrant 1  $u' > 0; w' > 0$  outward interaction
- Quadrant 2  $u' > 0; w' < 0$  sweep
- Quadrant 3  $u' < 0; w' < 0$  inward interaction
- Quadrant 4  $u' < 0; w' > 0$  ejection

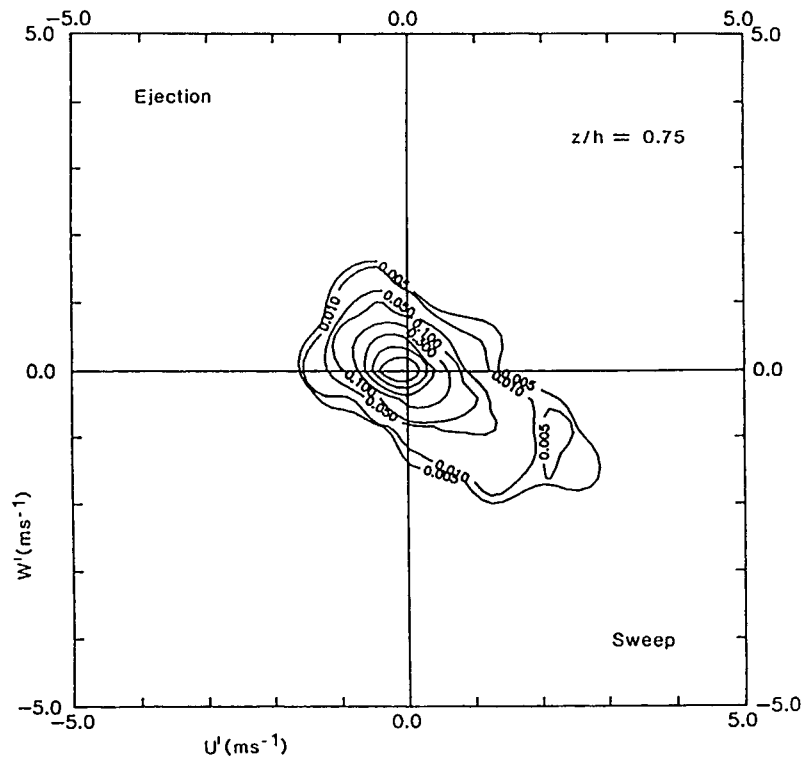
while the 'hole' refers to the exclusion from the integral of values of  $|\overline{u'w'}|$  less than some threshold  $H$ , so that the typical size of 'events' contributing to the flux can be gauged. The technique has been most commonly applied to  $\overline{u'w'}$  but also, frequently, to the heat flux  $\overline{w'\theta'}$  and occasionally to the carbon dioxide and moisture fluxes. Some investigators have measured the complete  $u' - w'$  pdf function (e.g., Shaw et al 1989, Maitani & Shaw 1990, Gardiner 1994). While this approach furnished more detailed information than Q-H, their results confirm rather than challenge the picture that has emerged.

What is consistently found in canopy studies is that the major contributor to momentum transfer within and just above the canopy is the sweep quadrant, representing the penetration of the canopy by fast, downward moving gusts ( $u' > 0; w' < 0$ ). The next most important quadrant is the ejection ( $u' < 0; w' > 0$ ). The contributions of the positive quadrants 1 and 3 are generally small except in coherently waving cereal canopies (Finnigan 1979, and see the discus-

sion in Shaw et al 1983). Figure 5, which displays the joint pdf of  $u' - w'$  measured at  $z/h = 0.75$  in a spruce canopy by Gardiner (1994), is typical of canopies generally. These results are in contrast to those obtained in smooth wall boundary layers, where the ejection quadrant is the major contributor to  $\overline{u'w'}$ , even near the wall. In rough wall boundary layers, however, sweeps begin to dominate as the rough wall is approached closely (Raupach et al 1991).

The second important finding to come from the application of Q-H was that the contributions to  $\overline{u'w'}$  by sweeps were individually very large, typically half the total contribution from sweeps coming from events greater than  $10|\overline{u'w'}|$ . Finally, these events were very intermittent with typically 50% of the stress being delivered in less than 10% of the time (Finnigan 1979, Shaw et al 1983). The results for shear stress are mirrored by those for heat flux, with sweeps once again responsible for most transport and occupying similarly small fractions of the total time (Coppin et al 1986, Gao et al 1989, Lee & Black 1993).

Quadrant-hole techniques yield information about the temporal structure of turbulent transfer at a single point. A different approach was required to reveal





spatial structure. By the late 1970s it was known that time series of scalars like temperature and humidity displayed characteristic 'ramp' structures that were well correlated above and through the canopy. It was a reasonable inference that these signals were the result of incursions of air from the boundary layer above rapidly flushing the canopy airspace. Denmead & Bradley (1985, 1987) were able to connect the ramps with rapidly changing concentration and windspeed profiles to illustrate the process graphically. This approach was made more quantitative, and the statistics greatly improved, by Shaw et al (1989) and Gao et al (1989) and, above a forest, by Bergstrom & Hogstrom (1989).

Gao et al (1989), in particular, by combining time-height plots of temperature and velocity vectors, were able to identify the scalar ramps with the sweeps that Q-H analysis had shown were responsible for transferring most of the shear stress. They confirmed that the sweeps were a feature of motions correlated throughout the roughness sublayer and, therefore, probably responsible for the large integral length scales resulting from two-point statistical analysis. Conditional sampling of spatially distributed features like velocity profiles had already been performed by Finnigan (1979), but it was the possibility of triggering sampling by the ramps in order to focus on times of intense turbulent transport that finally cemented the connection between the structures transporting scalars and those transporting momentum and showed that the same large, infrequent eddies were responsible for both, at least in flows near neutral stratification.

Reinforcing this deduction, Shaw et al (1989) combined three detection methods based on the temperature field in a forest (variable interval time averaging—VITA, a new approach that required a temperature ramp to be present at several heights and direct inspection of the time traces) with two new methods based on the two-dimensional ( $u', w'$ ) vector field. In these methods the  $u', w'$  velocity vector is rotated into a new coordinate frame aligned with the major and minor axes of the joint pdf of  $u'$  and  $w'$ . In these axes, ejection-sweep sequences display a characteristic signature. Their data showed that ramps generally but not always accompanied ejection-sweep cycles. Paw U et al (1992), concentrating on scalar ramps and comparing different detection schemes, were able to extend the approach to a wider range of canopies and stabilities.

A good example of the synthesis between temporal and spatial measurements that was achieved is Figure 6 from Gao et al (1989). It is a time-height cross section of ensemble averaged temperature and velocity fields measured in an 18-m-high deciduous forest. Twenty unequivocal ramp events from two different runs are combined in this plot and clearly show three things: The sharp temperature microfront that constitutes the steep edge of the ramp is coherent from mid canopy level to about  $2.5h$ ; within the upper half of the canopy the microfront is preceded by a weak upward movement of less than average velocity air (a momentum ejection) and succeeded by a strong incursion of high-velocity air (a momentum sweep); above the canopy this sequence is reversed, with a stronger ejection before the microfront being succeeded by a weaker sweep.

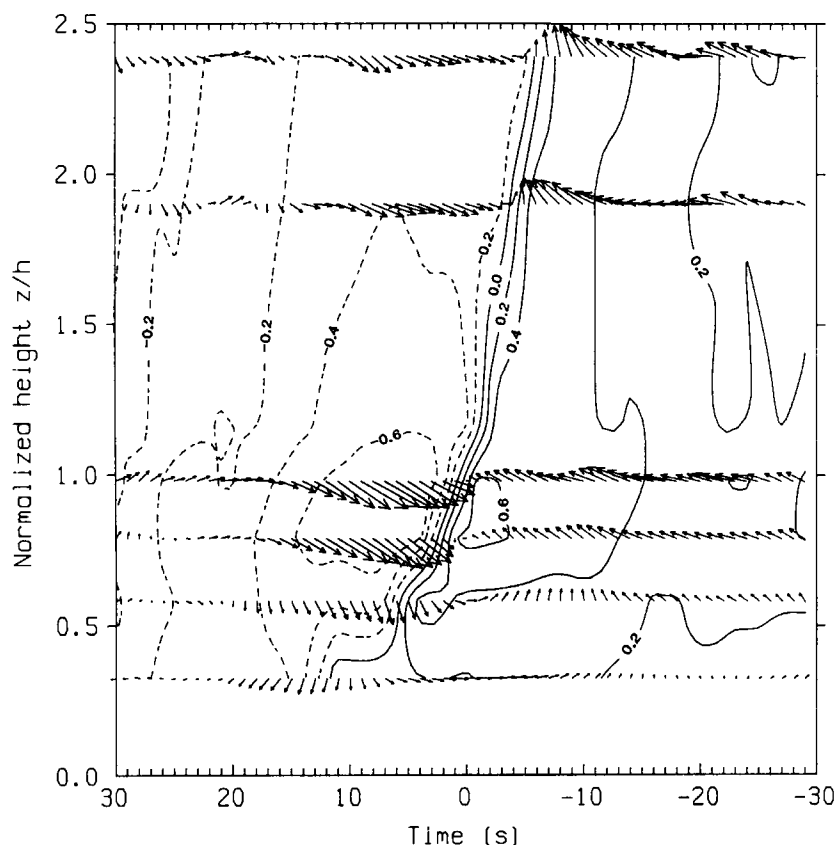


**Figure 6** Time-height plot of ensemble averaged temperature and fluctuating velocity fields measured in moderately unstable conditions ( $L = -138\text{m}$ , where  $L$  is Monin-Obukhov length) in a 18-m-tall mixed forest. Dashed lines are isotherms below the mean and solid lines are isotherms above the mean. Contour interval is  $0.2^\circ\text{C}$  and the maximum arrow length represents a wind magnitude of  $1.9\text{ ms}^{-1}$ . Figure from Gao et al (1989).

A further step forward in methodology came with the use of wavelet transforms to extract statistics of the characteristic features of scalar and velocity fields associated with ramps. Collineau & Brunet (1993) compared various wavelet shapes with more standard schemes (VITA and 'window averaged gradient'—WAG) and were able to remove some of the subjectivity that is always associated with conditional sampling schemes. Using data from a pine forest, they confirmed that scalar ramps are associated with the ejection-sweep sequence that transfers most of the momentum. Their conclusions were extended by Lu & Fitzjarrald (1994), who applied wavelet analysis to a much larger forest data set.

Figure 7 from Collineau & Brunet (1993) condenses much of what has been learned from conditional sampling into one figure. Using as a trigger the RAMP wavelet transform applied to the temperature signal only, they assembled conditional statistics of  $u'$ ,  $w'$ , and  $T' = \theta'$ . The conditional averages (denoted by  $\langle \rangle$ ) are ensemble averages of short sections taken from the time series of the variables. The sections were collected whenever a ramp face was present and extended from  $-15$  to  $+15$  seconds around the microfront. The two panels on the left-hand side of Figure 7 describe data from  $z/h = 1.24$ , whereas those on the right are from  $z/h = 0.82$ ; the graphs should be read from left to right. The upper two panels show the conditionally averaged signals themselves, and the main differences between the two levels lie in the greater asymmetry of the within-canopy signals around the microfront. The conditional products  $\langle u' \rangle \langle w' \rangle$ ,  $\langle u' w' \rangle$ ,  $\langle w' \rangle \langle T' \rangle$ , and  $\langle w' T' \rangle$  shown in the lower panels are more interesting. (Note that these products are normalized by the total flux magnitudes,  $|\overline{u' w'}|$  and  $|\overline{w' T'}|$ .)

First, they show the temporal progress from ejection to sweep at both levels and for both momentum and heat flux. Second, they show that sweeps make a much larger relative contribution within the canopy than above, the ratio of the total stress fraction transferred by sweeps to that by ejections being 1.04 at  $z/h = 1.24$  and 2.43 at  $z/h = 0.82$ . These ratios are consistent with those found in the conventional Q-H analyses discussed above. Third, we see that the total flux  $\langle u' w' \rangle$  and  $\langle w' T' \rangle$  is made up of a coherent part  $\langle u' \rangle \langle w' \rangle$ ,  $\langle w' \rangle \langle T' \rangle$  formed from the ensemble of conditionally averaged variables and a background contribution  $(\langle u' w' \rangle - \langle u' \rangle \langle w' \rangle)$ ,  $(\langle w' T' \rangle - \langle w' \rangle \langle T' \rangle)$ , resulting from turbulence that is not coherently related to the microfront. This background contribution comprises a roughly constant offset around the coherent part, allowing us to deduce that the ejection-sweep sequence is entirely associated with the phenomenon that causes the microfront.

### 4.3 Empirical Orthogonal Function Analysis

The work of Collineau & Brunet (1993) and of Lu & Fitzjarrald (1994) brought greater objectivity to the conditional sampling process, but this was still mainly in the time domain; a presumption about spatial structure was inherent in their approach as they used the presence of a scalar ramp or microfront as a selection trigger. A more objective approach to deducing the spatial structure of the dominant eddies has been taken by Finnigan & Shaw (2000), who have applied the techniques of empirical orthogonal function (EOF) analysis to a wind tunnel model canopy.

EOF analysis in the context of turbulent flows was introduced by Lumley (1967, 1981). It consists in finding the sequence of orthogonal eigenfunctions and associated eigenvalues that converges optimally fast when the variance or kinetic energy of the turbulent flow is represented as the sum of this sequence. The spatial structure of the turbulent field is contained in the eigenfunctions, and the rate of convergence of the sequence of eigenvalues is a sensitive indicator of the presence

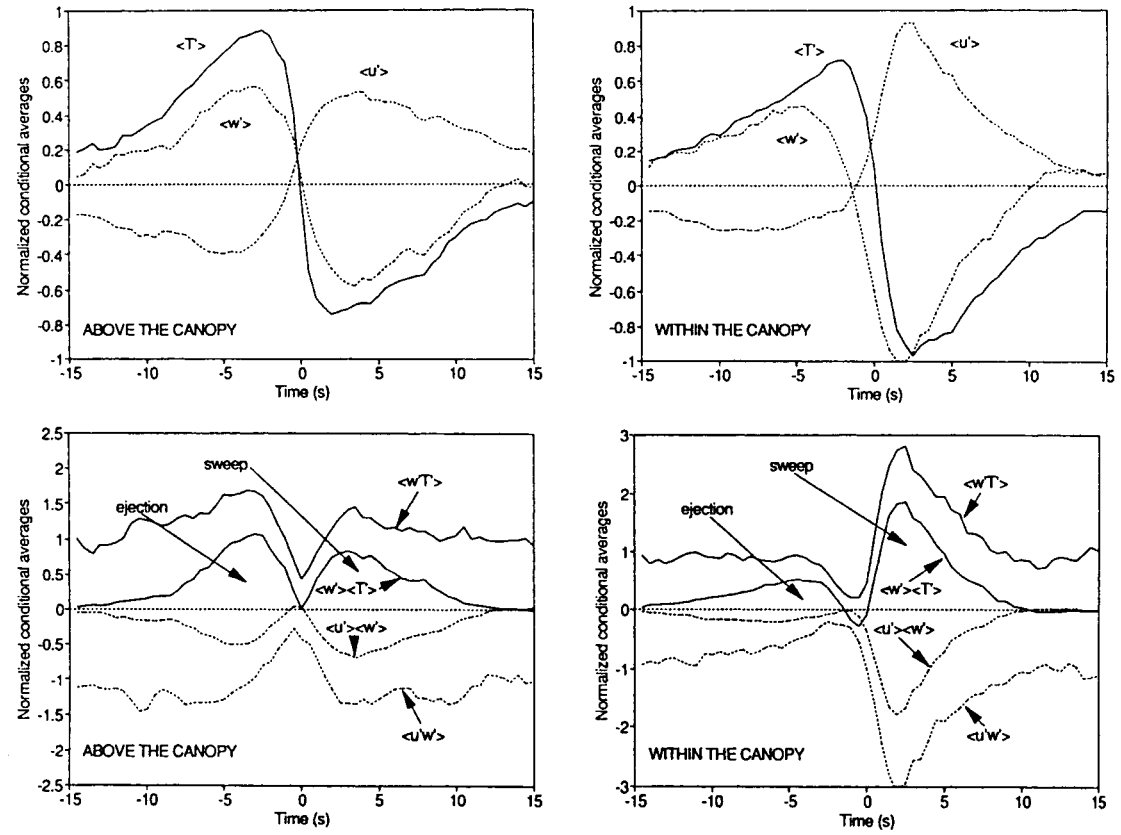


**Figure 7** Conditional averages of  $u$ ,  $w$ ,  $T$  ( $=\theta$ )  $uw$  and  $wT$  obtained in a pine forest. Sampling was triggered using the RAMP wavelet transform on temperature time series above the canopy and a conditional average is denoted by  $\langle \rangle$ . Cross products of  $\langle u' \rangle \langle w' \rangle$  and  $\langle w' \rangle \langle T' \rangle$  are also displayed.  $\langle u'w' \rangle$ ,  $\langle u' \rangle \langle w' \rangle$ ,  $\langle w'T' \rangle$  and  $\langle w' \rangle \langle T' \rangle$  are normalized with  $|u'w'|$  and  $|w'T'|$ , respectively. Figure from Collineau & Brunet (1993).

and relative importance of coherent structures. In shear flows dominated by coherent motions, a large fraction of the variance or TKE is captured in just the first few eigenmodes, whereas in flows with no dominant structure the rate of convergence is slower. A great strength of the method is that only trivial assumptions about the form of the dominant structure need be made a priori, so that we obtain essentially objective knowledge about the spatial structure of the coherent motion. In introducing the application of the technique to turbulent flows, Lumley (1981) gives a thoughtful discussion of the relative merits and drawbacks of conditional sampling and the EOF method.

Despite the advantages of the EOF method, it has not yet been widely used in turbulent flows because the required empirical eigenfunctions are those of the two-point velocity covariance tensor  $R_{ij}(\mathbf{x}, \mathbf{x}') = \overline{u'_i(\mathbf{x})u'_j(\mathbf{x}')}$  with spatial separation in three dimensions, a data set whose collection requires a particularly intensive experiment; thus, the technique has been applied to numerical simulations as much as to real data. Moin & Moser (1989), for example, performed an EOF analysis of a numerical simulation of channel flow, and their paper is an excellent introduction to the technique. Finnigan & Shaw (2000) used as their data set the two-point covariance field described by Shaw et al (1995), examples of which we have already presented in Figure 3.

The EOF technique can be applied in one, two, or three dimensions. In one dimension the empirical eigenfunctions  $\phi_i(z)$  are solutions of

$$\int_D R_{ij}(z, z') \phi_j^*(z') dz' = \lambda \phi_i(z), \quad (4.3)$$

where  $R_{ij}(z, z') = \overline{u'_i(z)u'_j(z')}$  is the two-point covariance tensor and \* denotes complex conjugate. The eigenvectors  $\phi_i^{(n)}(z)$  form a complete set; that is the original random vector field  $u'_i(z)$  can be reconstructed from the eigenvectors

$$u'_i(z) = \sum_n a_n \phi_i^{(n)}(z), \quad (4.4)$$

where the coefficients  $a_n$  are random in the sense that a set of  $a_n$  belongs to each realization of the random field  $u'_i(z)$ . Because the kernel of the eigenvalue problem is the time-averaged covariance tensor, we only know  $a_n$  in a mean square sense as the eigenvalues

$$\overline{a_n a_m^*} = \begin{cases} \lambda^{(n)} & (n = m) \\ 0 & (n \neq m) \end{cases}. \quad (4.5)$$

A consequence of Equations 4.4 and 4.5 is that the turbulent stresses can be determined from the eigenvectors and eigenvalues

$$\overline{u'_i u'_j} = \sum_n \lambda^{(n)} \phi_i^{(n)}(z) \phi_j^{(n)*}(z). \quad (4.6)$$

Together with a normalization condition on the eigenvectors, the set of equations (4.3–4.5) constitute the Karhunen-Loève decomposition of the vector field  $u'_i(z)$

(Lumley 1981). The individual eigenvectors are optimal in the sense that, when ranked in order of decreasing magnitude of their eigenvalues, the first eigenvector captures as much as possible of the variance of the random field,  $u'_i(z)$ . The second captures as much as possible of the remaining variance, and so on. We expect, therefore, that in a field dominated by a distinct spatial pattern or characteristic eddy, the convergence of the series of eigenmodes will be much more rapid than otherwise, and, indeed, the rate of convergence of the sequence can be used as an objective test of the presence and importance of such structures.

Finnigan & Shaw (2000) compared the contribution of partial sums of the eigenmodes to the vertical distributions of  $\overline{u'^2}$ ,  $\overline{w'^2}$ ,  $\overline{u'w'}$  in both the roughness sublayer alone ( $z = 0-2h$ ) and the lower surface layer plus roughness sublayer ( $z = 0-6h$ ). They found that convergence was indeed significantly more rapid in the roughness sublayer than in the surface layer. While their results offered objective evidence that the turbulence in the roughness sublayer is dominated by more distinct eddy structures than in the surface layer above, the most interesting contribution EOF analysis makes is through its extension to two and three dimensions.

First, we note that if we simply extend the eigenvalue problem Equation 4.3 to three dimensions by replacing the covariance tensor by its three-dimensional form,  $R_{ij}(\mathbf{x}, \mathbf{x}')$ , then we would find that the Karhunen-Loève eigenvectors in the homogeneous  $x$  and  $y$  directions are simply Fourier modes, that is, the eigenmodes would have the form,

$$a_n(k_x, k_y) \phi_i^{(n)}(k_x, k_y, z) \exp i(k_x x + k_y y). \quad (4.7)$$

Just as in Equation 4.4 above, we could reconstruct realizations of the original velocity field by summing a sequence of modes (4.7). The random coefficients  $a_n(k_x, k_y)$  now contain information about both the amplitudes of the eigenvectors and the relative phases of their Fourier modes. Unfortunately, because we have obtained the eigenmodes from the time-averaged covariance tensor, we have lost this phase information and only know the coefficients  $a_n(k_x, k_y)$  in a mean square sense, i.e. as the eigenvalues,

$$\overline{\hat{a}_n(k_x, k_y) \hat{a}_m^*(k_x, k_y)} = \begin{cases} \lambda^{(n)}(k_x, k_y) & n = m \\ 0 & n \neq m \end{cases} \quad (4.8)$$

The contribution of the eigenmodes to second order statistics can be determined without knowledge of the phases, however, and Finnigan & Shaw (2000) found that the spatial information in the covariance tensor  $R_{ij}(\mathbf{x}, \mathbf{x}')$ , for example, the patterns shown in Figure 3a and 3b as well as over 90% of the TKE in the roughness sublayer was captured by the first five of the total of 42 eigenmodes. Following Moin & Moser (1989), they reasoned that the information contained in these first five eigenmodes could be used to construct a typical member of the family of coherent eddies that dominated the covariance patterns. This 'characteristic eddy' would have the form,

$$u_i^c(x, y, z) = \sum_1^5 a_n(k_x, k_y) \phi_i^{(n)}(k_x, k_y, z) \exp i(k_x x + k_y y). \quad (4.9)$$

The amplitudes of a typical set of coefficients  $a_n(k_x, k_y)$  are simply the square roots of the eigenvalues, but the lost information on the phases cannot be recovered from the EOF process. Instead, it is necessary to make two further hypotheses: that individual eddies are randomly distributed on the  $(x-y)$  plane and that individual eddies are compact in space (Finnigan & Shaw 2000, Moin & Moser 1989, Lumley 1981). With these relatively weak additional assumptions, Finnigan & Shaw were able to construct the vector field of a characteristic eddy on the  $(x-z)$  and  $(y-z)$  planes. This characteristic eddy should be viewed as the most likely member of the total population of eddies that went to form the covariance tensor.

Figure 8 from Finnigan & Shaw (2000) is the projection of  $u_i^c$  onto the  $(x-z)$  plane. Note that this is the perturbation velocity field of the characteristic eddy; to obtain the total instantaneous velocity, we must add the background mean field  $\bar{u}(z)$ . Figure 8 clearly shows a weak updraft or ejection around  $x/h = 5.0$ , followed by a strong sweep with maximum velocities around  $z/h = 1.25$ . Within

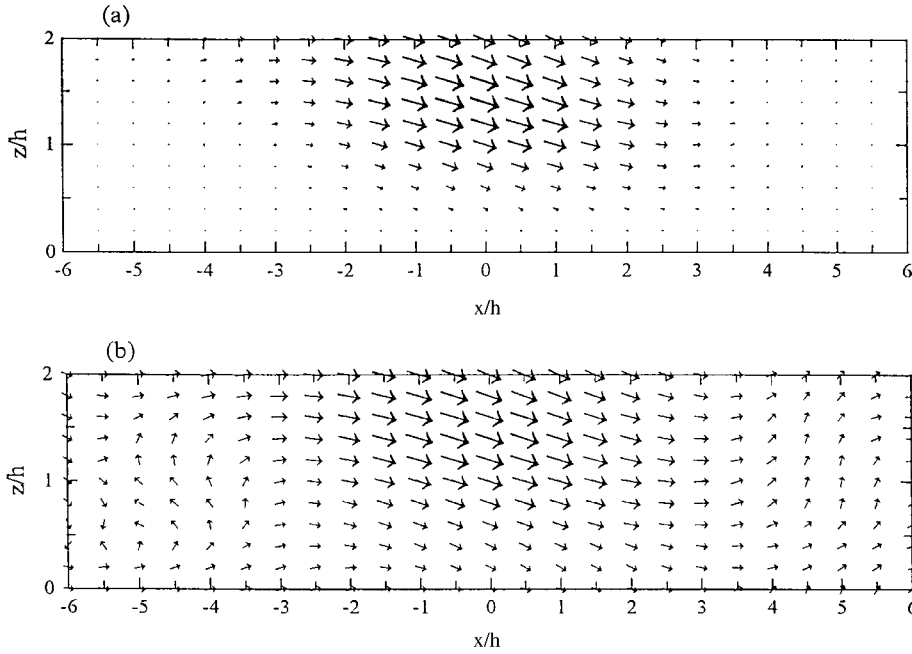


**Figure 8** The  $u', w'$  vector field of the characteristic eddy projected onto the  $(x, 0, z)$  plane. Figure from Finnigan & Shaw (2000). (a) Arrow lengths are proportional to velocity vector magnitudes; (b) As in (a) but with arrow lengths of low velocity regions magnified to show flow directions more clearly.

the canopy the sweep is more localized in the  $x$  direction than just above the canopy, being confined between  $x/h \approx \pm 1.0$ , and the whole sweep event is followed by a region of incoherent or almost stagnant flow between  $-4.0 > x/h > -6.0$ .

This velocity pattern corresponds quite closely to the ensemble averaged velocity fields shown in Figure 5 and to similarly constructed fields obtained by Gardiner (1994) (see his Figure 6). The pattern of weak ejection followed by a strong sweep also corresponds quite well to the conditional ensemble averages of Collineau & Brunet (1993) shown in Figure 7.

By exploiting the fact that the characteristic eddy is much more compact in the lateral than in the streamwise direction, Finnigan & Shaw were able to construct the projection of  $u_i^c$  onto the  $(y-z)$  plane. This projection, shown in Figure 9, has several interesting and unexpected features. First we point out that the bilateral symmetry of  $u_i^c$  is forced on the characteristic eddy by the symmetry of the covariance tensor,  $R_{ij}(\mathbf{x}, \mathbf{x}')$ , and this in turn is dictated by the experimental configuration. We would not expect any individual member of the real population of coherent eddies to be exactly symmetrical; our characteristic eddy is reflecting the ensemble average symmetry of the whole population.

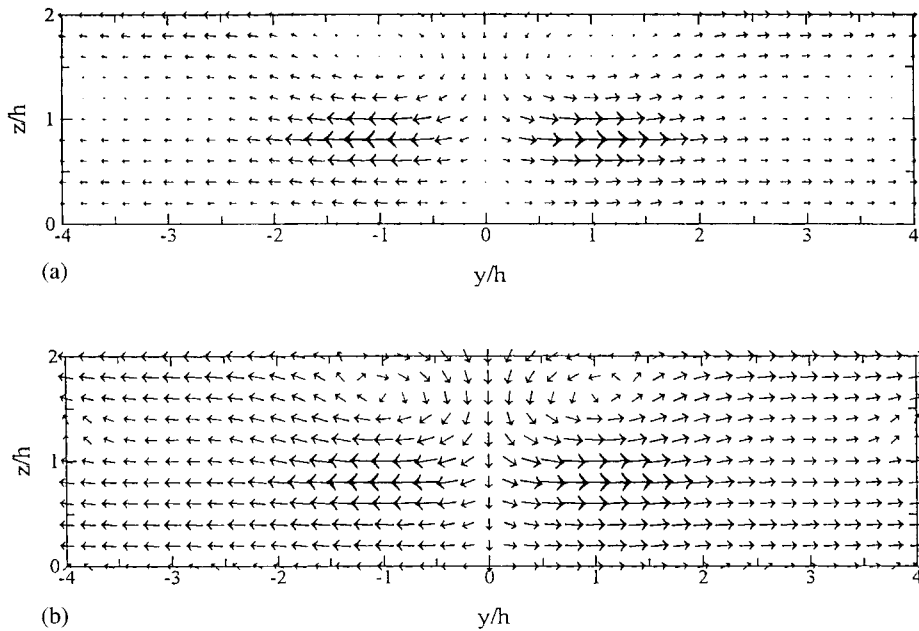


**Figure 9** The  $v', w'$  vector field of the characteristic eddy projected onto the  $(0, y, z)$  plane. Figure from Finnigan & Shaw (2000). (a) arrow lengths are proportional to velocity vector magnitudes; (b) As in (a) but with arrow lengths of low velocity regions magnified to show flow directions more clearly.



Interpreting Figure 9 in conjunction with Figure 8, we see that the strong downsweep of Figure 8 is confined to the region of  $y/h = \pm 0.5$  and penetrates only the upper third of the canopy before spreading sideways in strong outflows extending to  $y/h = \pm 2.0$ . The velocity pattern is consistent with a pair of counter-rotating vortices with their centers at  $(y/h, z/h = \pm 1.0, 1.6)$ . The velocity pattern is also consistent (as it should be) with the distinctly different extents of the regions of strong  $u'-u'$  and  $w'-w'$  correlation discussed in section 4.1, the strong vertical motion being confined to the region between the vortex pair around  $x = 0$ .

The sense of rotation of the vortex pair is opposite to that found by Moin & Moser (1989) in the wall region of their channel flow simulation. One mechanism often advanced for the formation of double roller eddies in boundary shear flows is the kinking of spanwise mean vortex lines by ambient turbulence, followed by their stretching in the strain field of the mean shear. See for example the various conceptual models of the ejection-sweep process described by Robinson (1991). This naturally results in the production of an inclined streamwise vortex pair with rotation in the sense opposite to Figure 10, but the same as those of Moin & Moser (1989). We see in the next section that a distinctly different mechanism may be responsible for the vector field of  $u_i^c$ .

## 5. THE MIXING-LAYER HYPOTHESIS

It is evident not only that the statistics of turbulence in the roughness sublayer are quite different from those in the surface layer above, but that the large-eddy structure deduced by conditional sampling and EOF analysis also has distinct differences. A decade ago, Raupach et al (1989) proposed that these differences can be explained by taking the plane mixing layer rather than the boundary layer as a pattern for roughness sublayer turbulence. They developed this mixing-layer hypothesis further and presented more evidence to support it in Raupach et al (1996).

### 5.1 The Plane Mixing Layer

The plane mixing layer is the free shear layer that forms when two airstreams of different velocity, initially separated by a splitter plate, merge downstream of the trailing edge of the plate. Flows of this kind are common in engineering applications and have been intensively studied. Figure 10 summarizes many of the generic properties of the mixing layer. Conventionally, the splitter plate occupies the horizontal half plane, ( $x < 0, z = 0$ ), and the difference between the free stream velocities above and below the plate is  $\Delta U$ . The width of the mixing layer can be characterized by the vorticity thickness  $\delta_\omega = \Delta U / (\partial \bar{u} / \partial z)_{\max}$  as shown in Figure 10. Even if the boundary layers each side of the splitter plate are laminar at  $x = 0$ , the mixing layer rapidly becomes turbulent and self-preserving when  $\delta_\omega \approx (x - x_0)$ , where  $x_0$  is a virtual origin (Townsend 1976).

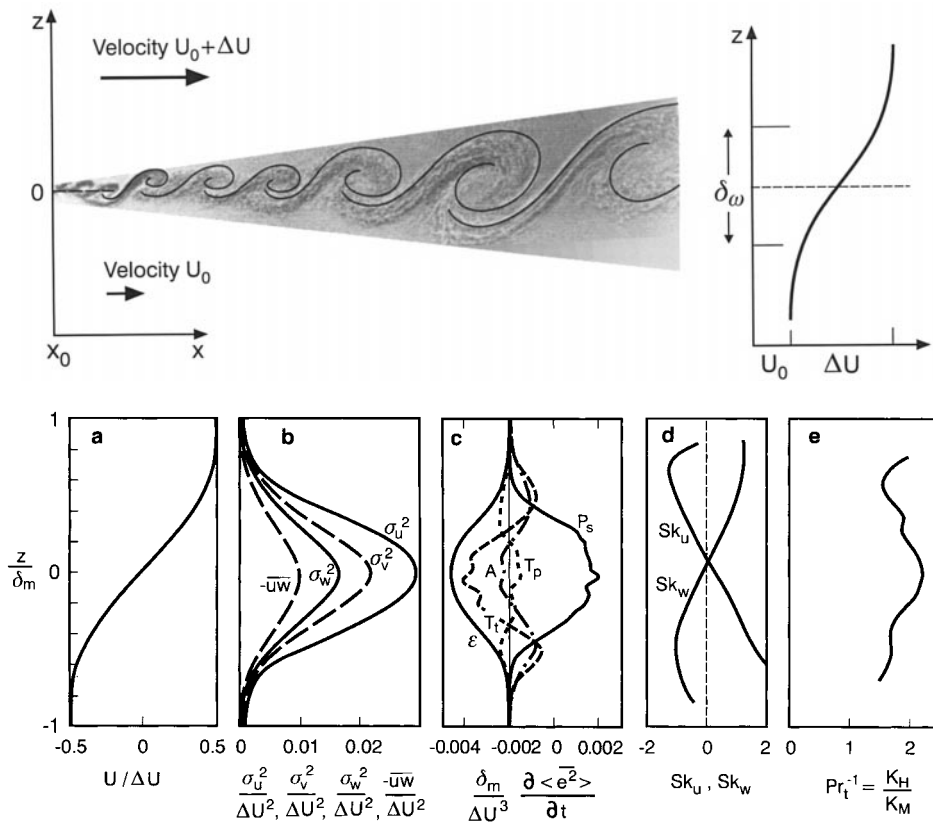


**Figure 10** Composite plot defining the parameters and flow statistics in the self-preserving region of a plane mixing layer. Variables are normalised with vorticity thickness  $\delta_\omega$  and velocity difference  $\Delta U$ . (a)  $U = \langle \bar{u}_1 \rangle$ ; (b)  $\sigma_u^2, \sigma_v^2, \sigma_w^2$  and  $-\overline{u'w'}$ ; (c) TKE budget terms as in equation (7.1); (d)  $Sk_u, Sk_w$ ; (e) inverse turbulent Prandtl Number,  $Pr_t^{-1}$ . Figure from Raupach et al (1996).

Referring to Figure 10a–e, we have plotted various properties of fully developed, self-preserving mixing layers, scaling the vertical coordinate  $z$  by  $\delta_\omega$  and the velocity moments by  $\Delta U$ . In Figure 10a we see the infection point in the mean velocity profile that is characteristic of mixing layers. The turbulent velocity variances  $\sigma_u^2$ ,  $\sigma_v^2$  and  $\sigma_w^2$  and the shear stress  $-\overline{u'w'}$  (see Figure 10b) all peak at the position of maximum shear,  $z = 0$ , and then decay toward the edge of the layer. The terms of the TKE budget, plotted in Figure 10c, correspond to those in Equation 7.1 below. There are significant turbulent and pressure transport terms exporting TKE to the outer fringes of the layer from the position of maximum shear production on the centerline. Note also that in the spatially growing mixing layer, horizontal advection is significant. In Figure 10d we observe that stream-

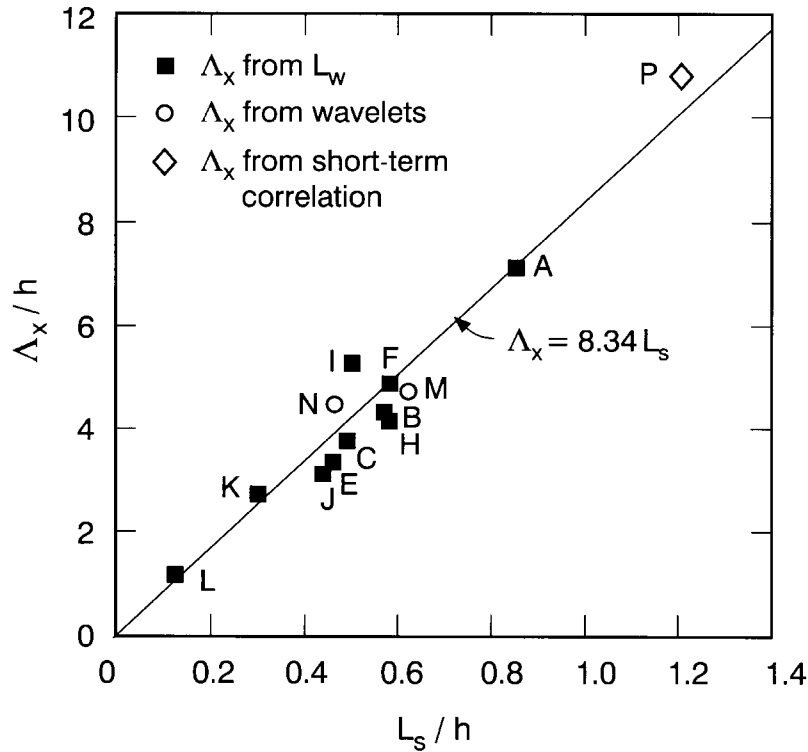


**Figure 11** Mean streamwise separation,  $\Lambda_x$  of coherent eddies near  $z = h$  plotted against shear length scale  $L_s$ . Both axes are normalized with  $h$ . For canopies A to L (Table 1),  $\Lambda_x$  is estimated from  $L_w(h)$ . For canopies M and P,  $\Lambda_x$  is estimated from wavelet event detection on  $w'$  signal. For canopy Q,  $\Lambda_x$  is estimated from short-time two-point  $u$  correlations. The straight line is a least squares regression forced through zero. Figure from Raupach et al (1996).

wise and vertical skewnesses are of order one in the outer parts of the mixing layer, reversing sign as the centerline is crossed, and finally in Figure 10e that the (inverse) turbulent Prandtl number is close to 2.

Mixing layers are also populated with coherent motions that span the depth of the layer. These were first recognized in the classic experiment of Brown & Roshko (1974), and since that time their structure and development have been intensively studied through analysis, numerical simulation, and in laboratory flows. The inflected velocity profile of the mixing layer is inviscidly unstable to small perturbations (Drazin & Reid 1981), and growing, unstable modes of Kelvin-Helmholtz type emerge in the early stages of mixing-layer development. This classical instability problem was studied by Michalke (1964, 1965), who

calculated the eigenvalues and eigenfunctions of the fastest growing modes. These modes rapidly grow past the bounds of small perturbation theory and, although the development of secondary transverse instabilities has been calculated by Pierrehumbert & Widnall (1982) in an extension of linear theory, most information on the subsequent development of the coherent motions has come from numerical studies. These studies are discussed in detail by Raupach et al (1996); here we give only a brief summary of the results.

We should note here that, while spatially growing mixing layers are what are generated in laboratory experiments, numerical simulations are usually of temporally growing layers, where the mean flow and initial turbulence levels are specified and the growing instabilities are homogeneous in space. Michalke (1964, 1965) performed small perturbation analyses of both situations and found only small differences in the fastest growing eigenmodes. The two situations are generally regarded as equivalent with time and horizontal distance being exchanged in intercomparisons. In both cases a universal sequence of instability processes leads to the final, fully developed turbulent mixing layer.

The initial Kelvin-Helmholtz waves rapidly evolve into distinct transverse vortices or rollers connected by braid regions. Whereas most of the transverse vorticity is concentrated in the rollers, the braid regions are areas of intense plane strain (Rogers & Moser 1994). Streamwise vorticity initially present in the flow is strongly amplified by strain in the braid regions. At the same time, neighboring transverse vortices begin to amalgamate stochastically leading to irregular streamwise spacing and growth of these vortices (Winant & Browand 1974). After several such pairings, the layer undergoes a distinct mixing transition corresponding to the onset of fully developed turbulence (Dimotakis & Brown 1976). The mixing layer becomes self-preserving shortly afterwards. After the mixing transition, the transverse rollers become kinked and are less organized (Browand & Troutt 1980, Comte et al 1992). Rogers & Moser (1994) found in their direct numerical simulation (DNS) of a temporally growing mixing layer that, if the initial turbulence level in the layer was high, then at later times, the transverse vorticity was weak; most of the total vorticity was concentrated in streamwise rib vortices in the braid regions and in the streamwise component of kinked rollers (see the HIROLL case of Rogers & Moser 1994).

The streamwise wavelength of the initial Kelvin-Helmholtz instability,  $\Lambda_x$ , is preserved through the stages of transition to fully developed turbulence and becomes the effective average spacing of the ultimate coherent structures. In a fully developed turbulent mixing layer, observations of  $\Lambda_x/\delta_o$  range from 3.5 to 5. These are somewhat smaller than the spacing predicted by linear perturbation theory, which expects  $\Lambda_x/\delta_o = 7.8$  for a spatially growing layer (Michalke 1965). Reasons for this discrepancy are discussed by Raupach et al (1996). Linear theory also predicts that the transverse extent of the secondary instability will be similar to the initial streamwise spacing  $\Lambda_x$ , the transverse wavelength of the most amplified mode being  $2/3\Lambda_x$  (Pierrehumbert & Widnall 1982).

## 5.2 The Canopy–Mixing Layer Analogy

The obvious feature of plane mixing layers that first prompted the comparison between them and canopy flows was the inflected mean velocity profile. Since it was known that this was inviscidly unstable to small perturbations, unlike the uninflected boundary layer profile, which only becomes unstable if viscosity is present, it was seen as a possible source of the high turbulence intensities in the roughness sublayer. The fact that the unstable eigenmodes were the same scale as  $\delta_\omega$ , a bulk measure of the profile, also seemed to offer a clue to the origin of the large eddies in the roughness sublayer. A direct comparison between the statistics of roughness sublayer turbulence reviewed in §3 and those of the low-speed half of the mixing layer discussed in §5.1 shows that roughness sublayer turbulence shares, to a compelling degree, the character of mixing layer rather than boundary layer turbulence. This comparison between single-point turbulence statistics in the three domains is summarized in Table 2.

We can go farther and make a direct comparison between features of the coherent structures in the roughness sublayer and the mixing layer, if we first state the relationship between the shear scale  $L_s$  and the vorticity thickness,  $\delta_\omega$ ,

$$L_s = \frac{\bar{u}(h)}{(\partial\bar{u}/\partial z)_{z=h}} \cong \frac{1}{2} \delta_\omega = \frac{1}{2} \frac{\Delta U}{(\partial\bar{u}/\partial z)_{\max}}. \quad (5.1)$$

Equation 5.1 is exact if the maximum shear is at  $z = h$  (which can serve as a dynamic definition of  $h$ ) and if we take the velocity deep within the canopy, where the shear is small (see Figure 1a), as equivalent to the free stream velocity on the low-speed side of the mixing layer. Observations of the spacing of coherent eddies in fully developed mixing layers then fall in the range  $10 > \Lambda_x/L_s > 7$ .

In Figure 11 we compare estimates of  $\Lambda_x$  obtained from nine of the canopies in Table 1 against the shear length scale  $L_s$ . Both axes are normalized with canopy height  $h$ . The estimates of  $\Lambda_x$  were obtained from the  $w'$  signal, as we assume

**TABLE 2** Comparison between the properties of canopy, surface-layer, and mixing-layer flows.

Property	Surface layer	Mixing layer	Canopy
Inflection in $\langle \bar{u}_1 \rangle(x_3)$	No	Yes	Yes
$\sigma_u/u^*$	2.5–3.0	1.8	1.8–2.0
$\sigma_w/u^*$	1.2–1.3	1.4	1.0–1.2
$r_{uw} = -\langle u'w' \rangle / (\sigma_u \sigma_w)$	$\sim 0.3$	$\sim 0.4$	$\sim 0.5$
$Pr_t = K_M/K_H$	$\sim 1.0$	$\sim 0.5$	$\sim 0.5$
Integral length scale	$\propto (z - d)$	$\propto \delta$	$\propto (h - d)$
$ Sk_u ,  Sk_w $	small	$O(1)$	$O(1)$
TKE budget	$Ps \cong \varepsilon$	large $Tt, Tp$	large $Tt, Tp$

that  $w'$  is more representative of purely active turbulence near the canopy top than is  $u'$ .  $\Lambda_x$  was obtained by three different methods: first, from the single point integral scale  $L_w$  with a correction for the difference between eddy convection velocity and the mean velocity (see section 4.1); second, from wavelet analyses; and third, from short-time, two-point velocity correlations. Full details can be found in Raupach et al (1996). It can be seen that the data over a very wide range of canopy types and scales closely fit the relationship  $\Lambda_x = 8.1L_s$ , which falls in the middle of the range for fully developed mixing layers. This is compelling evidence that the process controlling the generation of large coherent structures in the roughness sublayer is very similar to that in the plane mixing layer; further supporting argument can be found in Raupach et al (1996).

We can summarize the canopy–mixing layer analogy by reference to the schematic diagram, Figure 12:

- The first stage is the emergence of the primary Kelvin-Helmholtz instability. We suppose that this occurs when a large-scale gust or sweep from the boundary layer well above the canopy raises the shear at  $z = h$  above some threshold level at which the instability can emerge from the background turbulence. The growth rate of the mixing layer instability is proportional to the magnitude of the shear at the inflection point, whereas in the high Reynolds number canopy flow, the scale of the shear,  $L_s$ , is independent of windspeed, depending only on canopy height and aerodynamic drag.
- The second stage is the clumping of the vorticity of the Kelvin-Helmholtz waves into transverse vortices or rollers connected by braid regions of highly strained fluid. The spacing of the rollers is similar to the wavelength of the initial instability.
- Finally, secondary instabilities in the rollers lead to their kinking and pairing, while any ambient streamwise vorticity in the braid regions is strongly amplified by strain resulting in coherent structures the transverse and streamwise dimensions of which are of the same order, and most of whose vorticity is aligned in the streamwise direction, just as we found for the characteristic eddy revealed by EOF analysis in §4.3. Note that the highly schematicized coherent structure shown as the third panel of Figure 12 is based on diagrams in Rogers & Moser (1992).

This conceptual picture has some further consequences. Because we expect that the primary instability only emerges from the background when the shear at the canopy top exceeds some threshold, then the convection velocity of the ultimate coherent structures will be larger than the mean velocity. We imagine that the footprint of the sweep that raises the shear above the threshold will be of larger scale than  $\Lambda_x$ , so we should expect to see some streamwise periodicity in canopy eddies. Short sections of periodicity are revealed by short-time two-point space time correlations; by using this technique in a wheat canopy, Finnigan (1979) found that canopy eddies arrived in groups of three or four, each group

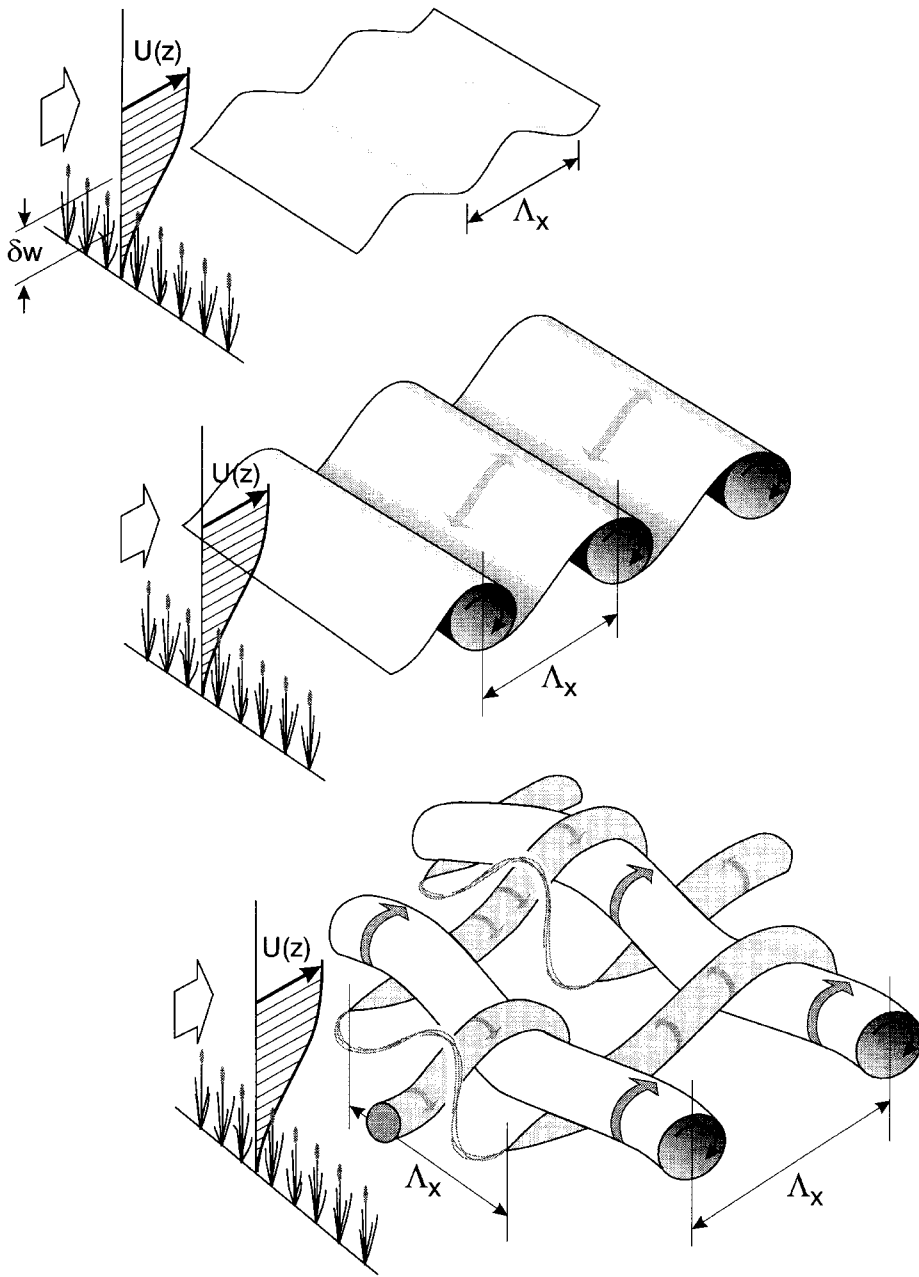


**Figure 12** Schematic diagram of stages in the development of the mixing-layer type instability in the roughness sublayer.

having a common convection velocity, corresponding presumably to the velocity of the large sweep that initiated the instability.

We can view the canopy instability process as the means by which momentum is removed from quasi-horizontal large-scale inactive motions in the lower boundary layer and transferred to the surface roughness. Raupach et al (1991) have suggested that in this sense canopy flows may form a model for rough surfaces in general. The mixing layer analogy also has obvious consequences for scaling and modeling canopy flow. A single length scale  $\delta_0$  and single velocity scale  $u^*$  or  $\langle \bar{u} \rangle(h)$  determine the primary instability and ultimate coherent structures in the roughness sublayer. Within the roughness sublayer, these scales replace the height-dependent length scale of the surface layer.

## 6. TURBULENT FINE STRUCTURE

From a purely fluid mechanical viewpoint, the feature that distinguishes canopy flows from more familiar boundary layer flows is that momentum is absorbed from the air stream as aerodynamic drag on the foliage over an extended vertical region rather than just at the surface plane. Simple and complex models of the wind field in such a situation always generate a concave or exponential velocity profile within the canopy that merges into the convex boundary layer profile above via the inflection point at  $z = h$  (Raupach & Thom 1981, Wilson & Shaw 1977). As we have seen, the character of this inflected profile ultimately determines the large eddy structure in the canopy, but the actual interaction of the flow and vegetation can be understood only by considering the fine-scale structure of canopy turbulence. This interaction not only results in aerodynamic drag, it also affects the eddy cascade, spectral shapes, viscous dissipation, and the TKE budget within the canopy.

### 6.1 Aerodynamic Drag

The aerodynamic force-per-unit-volume vector  $F_i(\mathbf{x}) = f_{Fi} + f_{Vi}$  appearing in the momentum Equation (2.7) consists of (minus) the sum of pressure and viscous forces on all the vegetation intersecting the averaging volume  $V$ . It is conventional to parameterize it as

$$F_i(\mathbf{x}) = -C_D(\mathbf{x})a(\mathbf{x})\langle \bar{u}_i \rangle |\langle \bar{u} \rangle|, \quad (6.1)$$

where  $|\langle \bar{u} \rangle| = \sqrt{\langle \bar{u}_i \rangle \langle \bar{u}_i \rangle}$ ,  $a(\mathbf{x})$  is the local foliage area per unit volume and  $C_D(\mathbf{x})$  is a drag coefficient. Focusing on an individual element in the averaging volume, we can write

$$F_{Fi}^{(EL)} = C_{DF}A_{FR} \langle \bar{u}_i \rangle |\langle \bar{u} \rangle|; \quad F_{Vi}^{(EL)} = C_{DV}A_{WE} \langle \bar{u}_i \rangle |\langle \bar{u} \rangle|, \quad (6.2)$$

where  $F_{Fi}^{(EL)}$  and  $F_{Vi}^{(EL)}$  are the kinematic pressure and viscous drag forces, respectively, on the element;  $C_{DF}$  and  $C_{DV}$  are element drag coefficients; and  $A_{FR}$  and



$A_{WE}$  are the frontal and wetted areas of the element. The drag coefficients depend on element Reynolds numbers  $Re = \langle \bar{u} \rangle L / \nu$ , where  $L$  is an appropriate element length scale. Values of  $Re$  range from  $10^5$  in the upper part of well-ventilated canopies to as low as  $10^2$  near the ground. Based on wind tunnel measurements in laminar airstreams,  $C_{DF}$  is approximately equal to 0.5 in the range  $10^5 > Re > 10^3$ , but it then roughly doubles as  $Re$  falls to  $10^2$ . In contrast,  $C_{DV}$  varies as  $Re^{1/2}$  over the entire range of  $Re$ .

Although the major component of drag on individual canopy elements will be pressure drag—for example Thom (1968) found that the ratio of pressure to viscous drag on bean leaves was typically 3:1—the contribution of viscous drag remains significant. So we expect to see significant dependence of  $C_D(\mathbf{x})$  on wind-speed, and indeed Brunet et al (1994) have reported large decreases in the drag coefficient of a wind-tunnel model canopy as the mean windspeed was increased. Similar observations in field canopies have in the past been ascribed to streamlining of flexible canopy elements in strong winds, but the  $Re$  dependence of the drag force provides a more satisfactory explanation.

When we compare  $C_D(\mathbf{x})$  measured in situ with the value we would expect from wind tunnel measurements of the drag on individual elements, we find the in situ drag coefficient to be smaller by factors of up to 3 or 4. This shelter effect is still not completely understood. Part of it is no doubt due to the fact that practical measurements within canopies overestimate the true volume-averaged velocity,  $\langle \bar{u}_i \rangle$  as attached boundary layers and near-wakes are inevitably under-sampled, but this cannot account completely for such large shelter factors. A much more likely explanation is that isolated-element  $C_D$ 's have not been measured in the very high turbulence levels and with the wide range of eddy scales that characterizes the local canopy environment. Seginer et al (1976), for example, compared the drag on elements in a wind tunnel model canopy with drag on the same canopy placed in a duct, where the large eddies of the roughness sublayer could not develop. In the duct flow, drag coefficients matched those on isolated elements, but in the canopy simulation they were almost four times smaller. Paradoxically, similar processes lead to scalar transfer coefficients within canopies that are much larger than their wind tunnel equivalents (Finnigan & Raupach 1987). The shelter effect is discussed in more detail and further references can be found in Raupach & Thom (1981), Finnigan & Raupach (1987), and Brunet et al (1994).

## 6.2 Spectra

Frequency spectra are our primary window on the fine structure of turbulence, and they have been measured in many different kinds of canopies, for example, in corn by Shaw et al (1974) and Wilson et al (1982), in forests by Baldocchi & Meyers (1988a) and Amiro (1990), and in wind tunnel models by Seginer et al (1976), Raupach et al (1986), and Brunet et al (1994). Canopy spectra were also reviewed by Kaimal & Finnigan (1994), while Seginer et al (1976) discussed

earlier spectral measurements. In Figure 13 we present power spectra of  $u'$ ,  $v'$ , and  $w'$ , obtained using sonic anemometers of 10-cm path length in Moga Forest, (Canopy F in Table 1). The power spectral densities  $S_u(f)$ ,  $S_v(f)$ , and  $S_w(f)$  are the Fourier transforms of the single-point, time-delayed autocovariance functions  $r_{aa}(\mathbf{x}, \tau; \mathbf{x})$ . The spectral densities satisfy

$$\int_0^\infty S_\alpha(f) df = \langle \overline{u_\alpha'^2} \rangle. \quad (6.3)$$

The spectra, each constructed by vertically averaging at least four 15-min time series and then logarithmically smoothing in frequency (Kaimal & Finnigan 1994, Chapter 7), are plotted as  $fS_\alpha(f)/\sigma_\alpha^2$  and the frequency axis is normalized with  $U_h/h$ . As we noted in section 3.2, the frequencies of the spectral peaks, which provide an inverse time scale for the energy-containing eddies, do not change as we descend into the canopy.

Kolmogorov's theory of universal equilibrium of high Reynolds number turbulence (Batchelor 1959) states that, if there is a sufficiently large gap between  $\Lambda$ , the length scale of the energy-containing turbulence, and the Kolmogorov scale  $\eta = (\nu^3/\epsilon)^{1/4}$  that characterizes the eddies directly involved in viscous dissipation ( $\epsilon$  being the viscous dissipation rate), then an inertial subrange (ISR) will exist, where the spectral densities take the form

$$S_\alpha(f) = \alpha_\alpha \epsilon^{2/3} f^{-5/3} \quad (6.4)$$

and where  $\alpha_\alpha$  are universal constants. Recent measurements by Saddoughi & Veeravalli (1994) suggest that a spectral gap of two to three decades between  $\Lambda$  and  $\eta$  is required for one decade of ISR to exist. Kolmogorov's theory is actually couched in terms of wavenumbers. To obtain Equation 6.4 we have assumed that Taylor's hypothesis can be used to convert between wavenumber and frequency space. There are problems with this assumption in the high turbulence intensities of canopy flows, and these are canvassed in some detail in Kaimal & Finnigan (1994). A second consequence of Kolmogorov's assumptions is that the turbulence in the ISR will be isotropic, which implies that  $S_v(f) = S_w(f) = 4/3 S_u(f)$  there.

In Figure 13 the spectra above the canopy exhibit a conventional inertial subrange with slopes of  $-2/3$  (as we are plotting  $fS_\alpha(f)$ ), but as we descend into the canopy the roll-off of  $S_u(f)$  is considerably faster than Kolmogorov theory would predict, the slope increasing with depth in the canopy.  $S_w(f)$  in contrast seems to roll off more slowly than  $-2/3$  in the canopy, whereas  $S_v(f)$  seems to match  $-2/3$  reasonably closely at all heights. These Moga spectra are quite representative of data obtained in forest and crop canopies.  $S_u(f)$  in almost all cases exhibits more rapid roll-off than  $-2/3$  within the canopy, but observations of  $S_w(f)$  and  $S_v(f)$  are more varied. Measurements by Amiro (1990), for example, showed that within a Spruce canopy all three components had steeper slopes than  $-2/3$ ; in an Aspen canopy  $S_u(f)$  and  $S_v(f)$  rolled off more steeply, while  $S_w(f)$

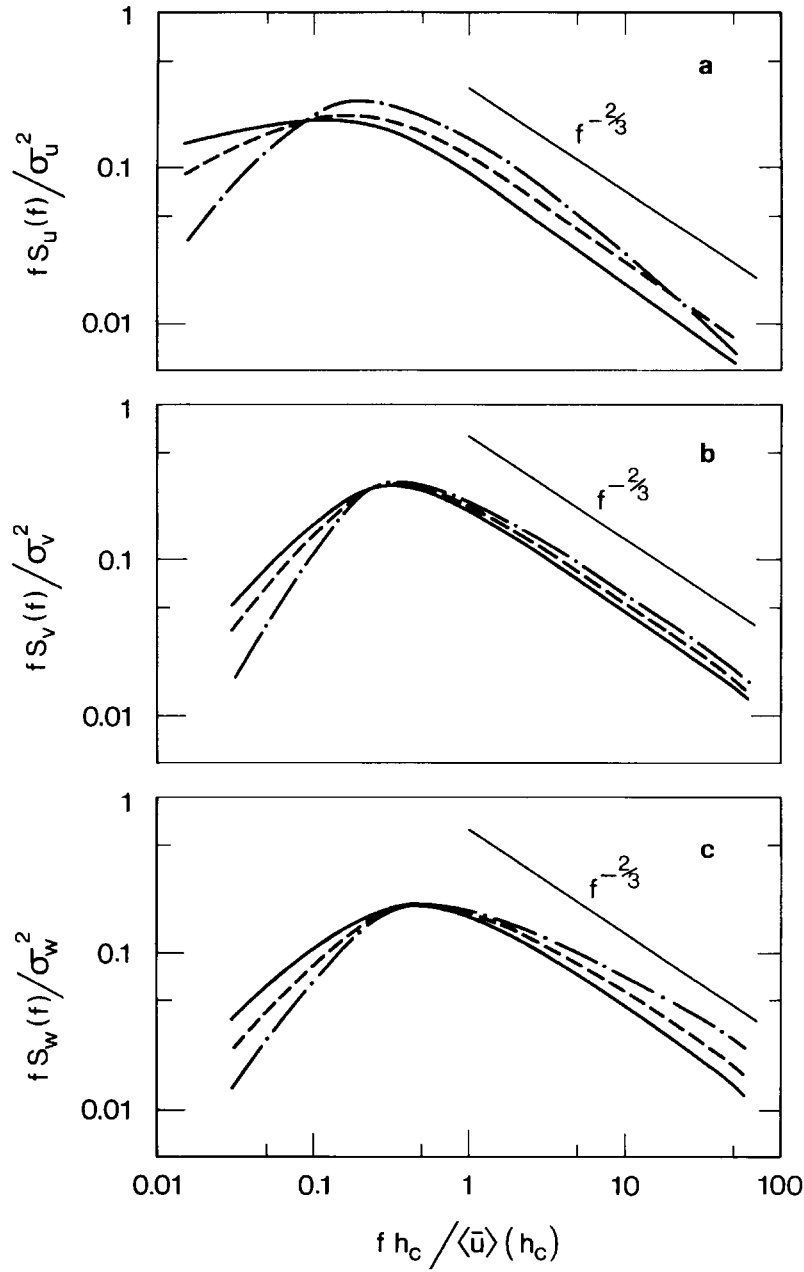


**Figure 13**  $S_u$ ,  $S_v$  and  $S_w$  frequency spectra obtained at three heights in Moga forest (Canopy F of Table 1).  $z/h = 1.5$  (—);  $z/h = 1.0$  (----);  $z/h = 0.5$  (— · —). Spectra are normalized with  $\sigma_u^2$  and frequencies with  $h_c/\bar{u}_{hc} = h/\langle \bar{u} \rangle$ . Figure from Kaimal & Finnigan (1994).

roughly matched  $-2/3$ ; while in a canopy of Pine, only  $S_u(f)$  had a slope significantly steeper than  $-2/3$ .

The expectation of isotropy seems to be satisfied above the canopy, but within, it is emphatically violated by most measurements. Comparing the spectral ratio,  $\beta = S_w(f)/S_u(f)$ , there is a good deal of scatter between canopies. In corn Shaw et al (1974) had  $\beta = 0.94$ , and  $\beta$  took a similar value in the dense deciduous forest of Baldocchi & Meyers (1988a). In Moga forest  $\beta = 1.7$ , and in Amiro's three canopies,  $\beta = 1.0 \pm 0.15$ .

This anisotropy and departure from the  $-5/3$  slope is not surprising when we compare the assumptions that are made in Kolmogorov's theory with canopy reality. To obtain Equation 6.4 we must assume first that in the inertial subrange TKE passes on average from lower to higher wavenumbers at a rate independent of wavenumber and equal to the dissipation rate  $\epsilon$ . There can be no processes adding or subtracting TKE from eddies within the ISR, only transfer of energy between wavenumbers in the eddy cascade. Second, the eddies occupying (in wavenumber space) the ISR are assumed to be sufficiently distant from the anisotropic energy-containing eddies and to have been through sufficiently many non-linear interactions that they have "forgotten" the anisotropy of the large scales. Within the ISR, therefore, there can be no processes that restore any anisotropic tendency to the eddies there. Neither of these conditions are fulfilled in the canopy.

In Figure 14 we present a schematic diagram of the processes affecting spectral behavior in the canopy. The diagram represents the energy spectrum function  $E(\kappa)$ , where  $\kappa$  is wavenumber magnitude and  $E(\kappa)$  satisfies

$$\int_0^\infty K(\kappa) d\kappa = \frac{1}{2} \langle \overline{u'_i u'_i} \rangle. \quad (6.5)$$

We have indicated on Figure 14 a major input of energy at the energy-containing wavenumber  $1/\Lambda$ . We have established that in the roughness sublayer this is primarily the result of the inflection-point instability process that removes energy from the mean flow and injects it into the coherent eddies. At the high wavenumber end of the spectrum, we see a steepening of slope as viscous dissipation begins to remove significant amounts of TKE and to convert it into heat. Both these processes occur in the free air above the canopy. Within the canopy two extra effects must be considered.

As the mean flow does work against the aerodynamic drag of the foliage, kinetic energy of the mean flow ( $MKE = 1/2 \langle \overline{u_i} \times \overline{u_i} \rangle$ ) is converted directly into heat and also into fine-scale turbulence in the wakes of canopy elements. Work against the viscous component of canopy drag converts MKE into heat, while work against pressure drag converts MKE into TKE at the scale of the wakes behind individual canopy elements. For convenience we term this fine-scale wake component of TKE, wake kinetic energy or WKE. It can represent a source of energy at higher wavenumbers than  $1/\Lambda$ . In wind tunnel model canopies, the distortion of the spectra caused by this injection of WKE can often be clearly

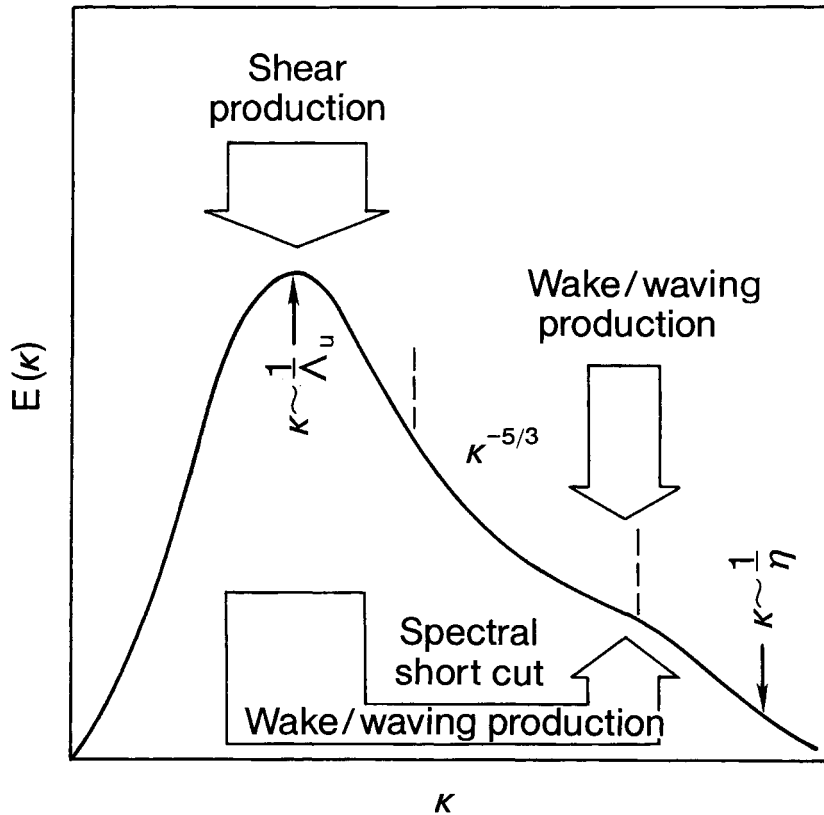


**Figure 14** Schematic diagram illustrating the extra processes that must be accounted for in theories of spectra in canopies.

observed; see for example Seginer et al (1976) and Raupach et al (1986). In these two cases the hot wire sensors used were able to resolve the dominant scales of WKE. In many natural canopies, however, particularly when sonic anemometers of 10–15-cm path length are employed, WKE of leaf scale is essentially invisible. In tall crops and forests, there is a large spectral gap between the wavenumber of leaf-scale WKE and the energy-containing scales; therefore in these canopies, WKE should only appear at the high wavenumber end of the ISR, but in many wind tunnel canopies most of the ISR will be seriously affected.

The second extra process, labelled on Figure 14 as a spectral short cut, represents exactly the same physical process but acting on turbulent eddies rather than the mean flow. Eddies of all scales larger than the canopy elements lose their TKE to both heat and WKE, and this represents a continual removal of energy from the eddy cascade, violating one of the fundamental assumptions behind Kolmogorov's  $-5/3$  law for the ISR. As we see below, this removal of energy

affects the different spectral components to different degrees, so that it also contradicts the assumption of isotropy. If we restrict ourselves to situations where the energy diverted to WKE by this mechanism ends up at the high wavenumber end of the ISR, then we can calculate how the spectral shape in the rest of the ISR will be affected by this spectral short cut.

The first step is to derive an expression for  $W_D(\mathbf{x})$ , the rate at which turbulent fluctuations do work against drag and lose kinetic energy to heat and WKE. If we assume that Equation 6.1 applies to these fluctuations as well as to the mean flow, we can write

$$W_D(\mathbf{x}) = \rho C_D(\mathbf{x}) a(\mathbf{x}) [\langle \overline{u u_i u_i} \rangle - \langle \overline{u_1} \rangle^3]; \quad |u| = \sqrt{u_i u_i}. \quad (6.6)$$

In Equation 6.6 the first term in the square brackets represents the rate of working against drag by the total flow field, while the second term is the rate of working by the mean flow  $\langle \overline{u_1} \rangle$  alone. Their difference is the rate of working by the turbulence. The presence of  $|u|$  in this formula means that it can only be expressed approximately in terms of integer velocity moments. The simplest approximation is obtained by expanding Equation 6.6 in a binomial series about  $\langle \overline{u_1} \rangle$  and retaining terms up to second order only, whence

$$W_D(\mathbf{x}) \cong \frac{3}{4} \rho C_D(\mathbf{x}) a(\mathbf{x}) \langle \overline{u_1} \rangle \langle \overline{u_i' u_i'} \rangle. \quad (6.7)$$

Note that approximation 6.7 will be innaccurate deep within the canopy, where the mean velocity approaches zero but the horizontal turbulent fluctuations remain significant. However, in the upper canopy, the approximation is commensurate with the assumption that Equation 6.1 applies to turbulent fluctuations.

To use this expression in computing changes in spectral shape in the ISR, we adopt a method first proposed by Pao (1965), who used it to calculate the form of the spectrum in the dissipation range. Let  $S(\kappa)$  be the rate at which TKE flows from wavenumbers less than  $\kappa$  to wavenumbers greater than  $\kappa$  in the ISR. Pao (1965) expressed  $S(\kappa)$  as

$$S(\kappa) = E(\kappa) \sigma(\kappa), \quad (6.8)$$

where  $\sigma(\kappa)$  can be regarded as the rate at which an energy spectral element is transferred across  $\kappa$ . The rate at which energy is gained or lost from a waveband  $\kappa - (\kappa + d\kappa)$  is equal to  $dS/d\kappa$ . Combining Equations 6.5 and 6.7, we can write for the  $\kappa$  range  $(1/\Lambda \gg \kappa \gg 1/l)$ , where  $l$  is a scale for the eddies formed behind plant elements:

$$\frac{dS}{d\kappa} = -\frac{3}{2} \rho C_D a \langle \overline{u_1} \rangle E(\kappa). \quad (6.9)$$

We now redefine  $\epsilon$  as the rate at which TKE reaches dissipation scales via the inertial eddy cascade through the ISR. It had been argued by Lumley (1964) that, if the rate of removal of TKE from waveband  $\kappa - (\kappa + d\kappa)$  by processes not

considered in Kolmogorov's theory is small compared to  $\epsilon$ , i.e. if  $\epsilon/(\partial\epsilon/\partial\kappa) \ll 1$ , then  $\epsilon$  does not change much through the ISR and still characterizes  $E(\kappa)$  there. We see below that this assumption can be justified for the ISR of canopy spectra. Adopting a similar viewpoint, Pao (1965) argued on dimensional grounds that  $\sigma(\kappa)$  in the ISR must take the form

$$\sigma(\kappa) = \alpha^{-1} \epsilon^{1/3} \kappa^{5/3}, \quad (6.10)$$

where  $\alpha$  is Kolmogorov's constant. Combining Equations 6.10 and 6.9, we obtain an equation for the form of the energy spectrum in the the ISR,

$$\frac{d}{d\kappa} (\alpha^{-1} \epsilon^{1/3} \kappa^{5/3} E(\kappa)) = -\frac{3}{2} C_D a \langle \bar{u}_1 \rangle E(\kappa). \quad (6.11)$$

Under the assumption that we recover the standard free-air form for  $E(\kappa)$  in the ISR as  $C_D a \rightarrow 0$ , the solution to Equation 6.11 is

$$E(\kappa) = \alpha \epsilon^{1/3} \kappa^{-5/3} \exp \left[ \frac{9}{4} C_D a \langle \bar{u}_1 \rangle \epsilon^{-1/3} \kappa^{-2/3} \right]. \quad (6.12)$$

In Figure 15 an illustrative comparison has been made between Equation 6.12 and the standard Kolmogorov form for the ISR,  $E(\kappa) = \alpha \epsilon^{2/3} \kappa^{-5/3}$ . The same value of  $\epsilon$  is used in both curves, the value chosen being  $u^{*3}/\kappa_v(h-d)$ . The values of  $u^*$ ,  $h$ ,  $d$ ,  $C_D$ , and  $a$  are chosen to correspond to the Moga forest canopy. We see that the modified energy spectrum rolls off considerably faster than  $-5/3$  at the low wavenumber end of the  $\kappa$  range but approaches  $-5/3$  as  $\kappa$  becomes large. This concave form for the spectrum can be observed in many of the within-canopy  $S_\alpha(f)$  spectra of Amiro (1990).

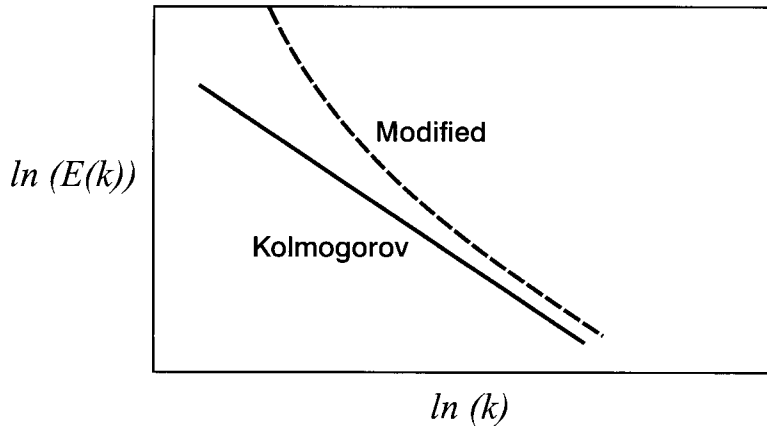


**Figure 15** The modified spectral shape in the inertial subrange obtained from Equation 6.12 using parameters appropriate to Moga Forest (Canopy F, Table 1). The standard Kolmogorov form for the same dissipation  $\epsilon$  is included for comparison.

While Equation 6.12 is indicative of the way that interaction with the vegetation changes the spectral form in the canopy, it is not very useful in a practical sense because measurements yield not  $E(\kappa)$  but component spectra  $S_\alpha(f)$  or equivalently  $S_\alpha(\kappa_i)$  after applying Taylor's hypothesis. Several more steps and assumptions are needed to obtain the modified forms of these measurable spectra. We briefly sketch these steps below:

1. We retain the truncated binomial form for  $W_D$  but now apply it to each velocity component separately:

$$\begin{aligned} W_{Du} &= 2\rho C_D a \langle \overline{u_1} \rangle \langle \overline{u_1'^2} \rangle; & W_{Dv} &= \rho C_D a \langle \overline{u_1} \rangle \langle \overline{u_2'^2} \rangle; \\ W_{Dw} &= \rho C_D a \langle \overline{u_1} \rangle \langle \overline{u_3'^2} \rangle. \end{aligned} \quad (6.13)$$

The asymmetry of the streamwise and cross-stream terms in (6.13) follows from the quadratic dependence of the pressure drag on the total velocity. The work against viscous drag in contrast affects all three velocity components symmetrically. Pressure drag-work asymmetry means that, throughout the wavenumber range affected, velocity moments and spectral functions may be homogeneous, but they are unlikely to be isotropic. The minimum symmetry that we can assume a priori is axial symmetry,  $x_1$  being the preferred direction. Further asymmetry can be imposed if the vegetation has a particular orientation so that the drag coefficient ( $C_D$ ) is different for different velocity components, but we ignore this effect here, assuming an isotropic drag coefficient. Note that the three terms in Equation 6.13 do not sum exactly to (6.7). Truncating the binomial expression for the total term (6.6) gives a slightly more accurate result than if we treat the terms individually.

2. The individual  $S_\alpha(\kappa_i)$  are obtained by integrating the tensor spectrum function of vector wavenumber  $\kappa_i$  with respect to  $\kappa_2$  and  $\kappa_3$  (Batchelor 1959),

$$S_\alpha(\kappa_1) = \int_{-\infty}^{\infty} \int_{-\infty}^{\infty} \Phi_\alpha(\mathbf{k}) d\kappa_2 d\kappa_3. \quad (6.14)$$

We choose the simplest general axisymmetric tensor form for the function  $\Phi_\alpha(\mathbf{k})$ . In an incompressible flow, this form has two free constants (Sreenivasen & Narasimha 1978).

3. To fix these constants we solve coupled equations for the streamwise and cross-stream spectral functions of scalar wavenumber,  $S_u(\kappa)$  and  $S_w(\kappa)$ , respectively,

$$\begin{aligned} \frac{d}{d\kappa} [(\alpha_1^{-1} \varepsilon^{1/3} \kappa^{5/3}) S_u(\kappa)] &= - \left( \frac{2c_1 \varepsilon}{\langle \overline{u_i' u_i'} \rangle} \right) \left[ S_u(\kappa) - \frac{1}{3} (S_u(\kappa) + 2S_w(\kappa)) \right] \\ &\quad - 2C_D a \langle \overline{u_1} \rangle S_u(\kappa) \\ \frac{d}{d\kappa} [(\alpha_3^{-1} \varepsilon^{1/3} \kappa^{5/3}) S_w(\kappa)] &= - \left( \frac{2c_1 \varepsilon}{\langle \overline{u_i' u_i'} \rangle} \right) \left[ S_w(\kappa) - \frac{1}{3} (S_u(\kappa) + 2S_w(\kappa)) \right] \\ &\quad - C_D a \langle \overline{u_1} \rangle S_w(\kappa), \end{aligned} \quad (6.15)$$



where  $\alpha_1 = 0.5$  and  $\alpha_3 = 0.66$  are the Kolmogorov constants for streamwise and cross-stream spectra, respectively. These equations differ from Equation 6.11 for the energy spectrum in two important respects: The last term in each equation is the spectral form of the anisotropic component drag work term (6.13); the equations are coupled by spectral pressure-velocity interaction terms, the first term on the right hand side of each equation (Batchelor 1959). We have used a very simple form for this term. It is essentially a spectral form of the 'return-to-isotropy' part of the standard pressure-strain interaction parametrization used in second order closure models of turbulence (Ayotte et al 1999). The constant  $c_1$  takes the standard surface layer value of 1.8 (Ayotte et al 1999).

4. Equation 6.15 can be solved analytically or numerically by an iterative method under the assumption that we recover the uncoupled, isotropic forms for the spectral functions as  $C_D a \rightarrow 0$ . The solutions converge quite rapidly,

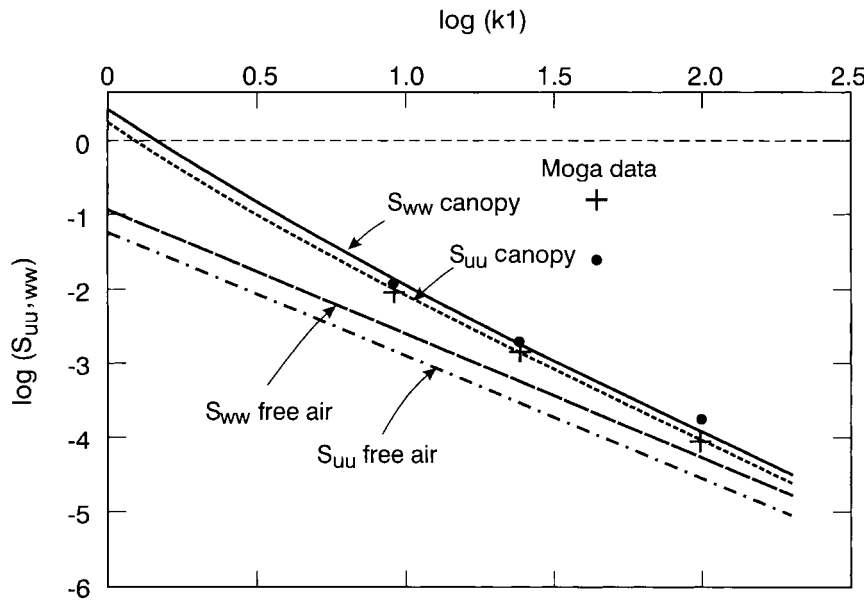


**Figure 16** Comparison of MKT theory with measured  $S_{uu} = S_u (+)$  and  $S_{ww} = S_w (\cdot)$  frequency spectra from Moga forest.  $\epsilon$  was determined for the two MKT curves by fitting the lowest frequency  $S_{uu}$  data point to the MKT result. The standard Kolmogorov curves for the same value of  $\epsilon$  (Equation (6.14)) are included for comparison.

and after two iterations about the uncoupled ( $c_1 = 0$ ) solutions, we are within 15% of the full numerical solution. For future convenience we refer to the four steps outlined above as the modified Kolmogorov theory or MKT.

In Figure 16 the solutions for  $S_u(\kappa_1)$  and  $S_w(\kappa_1)$ , converted to frequency spectra by Taylor's hypothesis, are compared with Moga forest spectra. The comparison was done by (a) choosing a value of  $S_u(f)$  from the Moga data, (b) calculating the value of dissipation  $\epsilon$  that corresponded to this point using analytic solutions of (6.15) in MKT with values of  $C_D a$  and  $\langle \overline{u_i^2} \rangle$  taken from the Moga data, (c) calculating complete curves of  $S_u(f)$  and  $S_w(f)$  from MKT, using the deduced value of  $\epsilon$ , and (d) observing whether other measured points from the Moga spectra fell on these lines. For comparison we include on the same graph curves of  $S_u(f)$  and  $S_w(f)$  obtained using the same  $\epsilon$  but the standard free-air formulae (6.4).

We see in Figure 16 that MKT appears to match the slopes of the streamwise and vertical spectra fairly well.  $S_u(f)$  rolls off slightly faster than the theory predicts, and  $S_w(f)$  more slowly. The theory also seems to get the anisotropy of the spectra reasonably correct, with the ratio  $\beta = S_w(f)/S_u(f)$  being close to the observations. A similar level of agreement is obtained for the wind tunnel model spectra of Brunet et al (1994), and it seems that despite the very simple assumptions involved in MKT the changed slopes and anisotropy of canopy ISR spectra can be largely explained in terms of the work done against drag, its anisotropy, and the pressure coupling of the component spectra. The variations in  $\beta$  observed between individual canopies may be a result of anisotropy in  $C_D$ , a factor not included in MKT. An important consequence of MKT is that, if we had deduced the dissipation rate by fitting the free air formulae rather than MKT, then we would have obtained  $\epsilon$  values roughly three times too large from the  $S_u(f)$  spectrum and 2.5 times too large from  $S_w(f)$ .

We are now in a position to justify the assumption leading to (6.10), that is, that the rate of removal of energy from the eddy cascade in the inertial subrange is small compared to the flux of energy through the ISR, i.e. that  $\epsilon/(\partial\epsilon/\partial\kappa) = \epsilon/W_D \ll 1$ . In fact the total amount of TKE flowing to dissipation scales via  $W_D$  over the entire spectrum is about five times as large as  $\epsilon$  (Shaw & Seginer 1985), but most of this energy comes from the energy-containing scales and in the inertial subrange  $\epsilon/W_D(\kappa) \cong 0.1$ . Thus we are justified in using a constant value for  $\epsilon$  in the modified ISR.

## 7.0 TKE Budget

Much of what we have discussed through this review is brought together by a consideration of the budget for the turbulent kinetic energy,  $1/2\langle \overline{u_i^2} \rangle$ . We obtain an equation for the TKE by taking the trace of (2.11),

$$\begin{aligned}
& \left( \frac{\partial}{\partial t} + \langle \bar{u}_j \rangle \frac{\partial}{\partial x_j} \right) \frac{1}{2} \langle \bar{u}'_i \bar{u}'_i \rangle = - \underbrace{\langle \bar{u}'_i \bar{u}'_j \rangle \frac{\partial \langle \bar{u}_i \rangle}{\partial x_j}}_{A} - \underbrace{\left\langle \bar{u}'_i \bar{u}'_j{}'' \frac{\partial \bar{u}_i''}{\partial x_j} \right\rangle}_{P_s} \\
& + \underbrace{\frac{g}{T_0} \langle \bar{u}'_3 \bar{\theta}' \rangle}_{P_b} - \underbrace{\frac{\partial \langle \bar{u}_j'' \bar{u}'_i \bar{u}_i''/2 \rangle}{\partial x_j}}_{T_d} - \underbrace{\frac{\partial \langle \bar{u}'_i \bar{u}'_i \bar{u}'_j \rangle/2}{\partial x_j}}_{T_t} - \underbrace{\frac{\partial \langle \bar{p}' \bar{u}'_j \rangle}{\partial x_j}}_{T_p} \\
& + \underbrace{\nu \frac{\partial^2 \langle \bar{u}'_i \bar{u}'_i \rangle/2}{\partial x_j \partial x_j}}_{T_v} - \underbrace{\nu \left\langle \frac{\partial \bar{u}'_i}{\partial x_j} \frac{\partial \bar{u}'_i}{\partial x_j} \right\rangle}_{\epsilon} + \text{waving terms.} \quad (7.1)
\end{aligned}$$

TKE budgets have been measured in a variety of canopies both in the field, e.g., Leclerc et al (1990), Meyers & Baldocchi (1991), and wind tunnel, e.g., Shaw & Seginer (1985), Raupach et al (1986), Brunet et al (1994). They have also been computed using a large eddy simulation (LES) model by Dwyer et al (1997). Figure 17a, measured in a wind tunnel model wheat canopy (Brunet et al 1994), displays features that are typical of the adiabatic situation. Note that Figure 17a differs from the corresponding Figure 17 of Brunet et al (1994) as some of the

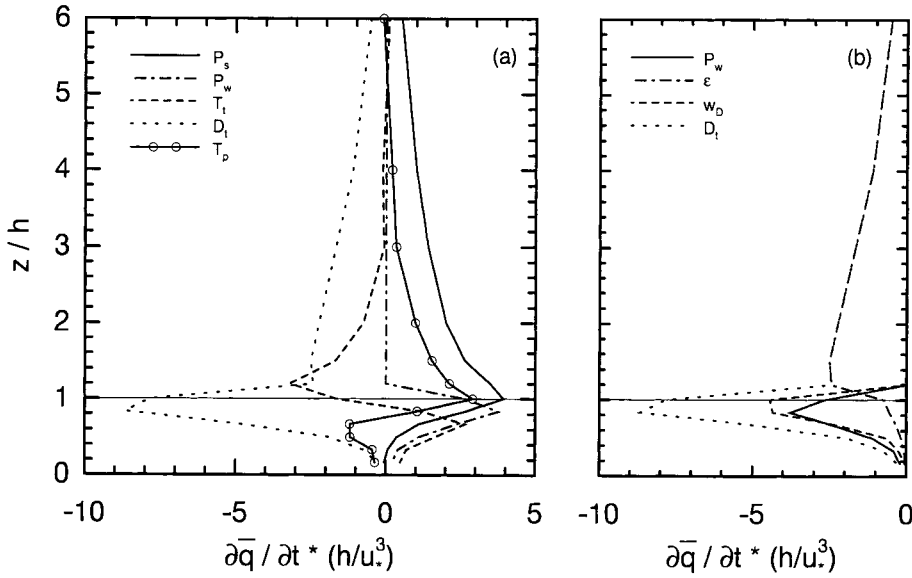


**Figure 17** (a) TKE budget in a model wheat canopy calculated from the data of Brunet et al (1994). Symbols refers to Equation 7.1. (b) Breakdown of the total dissipation term  $D_t$  into the negative of wake production,  $-P_w$ , the eddy cascade component  $\epsilon$  and the work done by turbulence against drag,  $W_D$ .

within-canopy terms have been recalculated with different assumptions. The model canopy was constructed of thin (0.25mm) flexible cylindrical elements, so that wake scales were not resolvable by the hot-wire anemometers used as sensors. As such its spectra and TKE budget are more typical of field than other wind tunnel canopies.

## 7.1 Production

At  $z = h$  we observe a strong peak in the shear production,  $P_s$  associated with the peak in shear and shear stress at the inflection point. Descending just below  $z = h$ , we encounter a large peak in the wake production  $P_w$ . This term is equal to the work done against pressure drag by the mean flow as this process converts MKE to WKE. For the thin elements of the model canopy, we estimate that viscous drag is about 20% of the total drag throughout the canopy, and  $P_w$  has been calculated as  $P_w = 0.8\rho C_D \bar{u} \bar{u}^3(z)$ . Raupach & Shaw (1982) showed that when dispersive and viscous transport is negligible, wake production is precisely equal to the work done by local steady perturbations in strain against local perturbations in Reynolds stress, the term identified as  $P_w$  in Equation 7.1. Except very close to the top of the canopy, it is the dominant production term.

## 7.2 Dissipation

The only complete treatment of dissipation in the canopy is that of Shaw & Seginer (1985), although it has been considered in the context of closure models by Wilson (1988) and Ayotte et al (1999). The very small eddies directly involved in viscous dissipation are rarely measured; instead we calculate the rate at which TKE is transferred to the scales ( $\sim \eta$ ) at which dissipation occurs. In the canopy, TKE arrives at these scales via three paths:

1. Wake production,  $P_w$ , the work done against pressure drag by the mean flow produces fine-scale WKE, bypassing most of the eddy cascade through the ISR. The characteristic time taken for wake scale eddies to transfer their energy to scales  $\sim \eta$  through the eddy cascade is very small (Shaw & Seginer 1985), so that we take the negative of  $P_w$  as the first contribution to total dissipation.
2. Larger scale turbulent eddies also lose energy to WKE as they do work against pressure drag through exactly the same mechanism as  $P_w$ . They also lose energy directly to heat as they do work against viscous drag. In the last section we derived simple expressions for  $W_D$ , the rate of working against total drag by TKE. Unfortunately, those formulae (6.7, 6.13) suffer from their dependence on the mean velocity as they underestimate drag-work deep within the canopy where  $\langle \bar{u}_1 \rangle$  is small but turbulence levels are large. To avoid this problem, Shaw (1977) assumed a Gaussian pdf for the velocity fluctuations in the canopy and obtained expressions for  $W_{D\alpha}$  in terms of the standard

deviations. Here we use a different formula derived by taking a binomial expansion of the exact expression around the total velocity and truncating at second order,

$$\begin{aligned}
 W_{Du} &= C_D(z)a(z) \{ [\langle \overline{u_1} \rangle^2 + \langle \overline{u'_1 u'_1} \rangle]^{1/2} [\langle \overline{u_1} \rangle^2 + \langle \overline{u'^2_1} \rangle] - \langle \overline{u_1} \rangle^3 \}; \\
 W_{Dv} &= C_D(z)a(z) [\langle \overline{u_1} \rangle^2 + \langle \overline{u'_1 u'_1} \rangle]^{1/2} [\langle \overline{u'^2_2} \rangle]; \\
 W_{Dw} &= C_D(z)a(z) [\langle \overline{u_1} \rangle^2 + \langle \overline{u'_1 u'_1} \rangle]^{1/2} [\langle \overline{u'^2_3} \rangle]; \\
 \text{and } W_D &= \frac{1}{2} (W_{Du} + W_{Dv} + W_{Dw}).
 \end{aligned} \tag{7.2}$$

Expression 7.2 agreed within 15% with exact computations of the individual components of (6.6) using data from Moga forest, and we use it to compute  $W_D$ , the second component of total dissipation.

3. TKE also is transferred inertially down the eddy cascade, but we saw in the last section that the standard Kolmogorov expression must be modified in order to calculate the amount of TKE reaching dissipation scales via this route. In the present case the result of this modification is to reduce the eddy cascade component  $\epsilon$  by one third on average throughout the canopy.

The three components of dissipation are shown separately in Figure 17b, and their sum is the total dissipation,  $Dt$  in 17a. We see that it is a very large term within the canopy. When interpreting it quantitatively though, we must remember that a series of simplifying assumptions were involved in estimating the three components.

### 7.3 Transport

The only transport term measured directly is turbulent transport  $Tt$ . This is a loss near the top of the canopy, where shear production peaks, and a gain in the lower canopy. Turbulent transport is effected by the large eddies that are coherent over the entire roughness sublayer space, and turbulent transport is a feature of both mixing layers and canopies. We cannot measure the other components of transport directly, but we assume that both dispersive and viscous transport are negligible and identify the residual in the budget with pressure transport,  $Tp$ . We see that the distribution of pressure transport is almost the mirror image of  $Tt$ . Its positive peak near  $z = h$  is slightly smaller than  $Tt$ , and its negative peak in the lower canopy is about half that of  $Tt$ .

Information about the behavior of  $Tp$  in canopies is contradictory. Four different approaches have been used to deduce  $Tp$ : as a residual as we have done above, by combining measured velocity and surface pressure (Maitani & Seo 1985), by calculating  $p'$  from the measured velocity field through an integration of the Poisson equation for pressure (Shaw et al 1990, Shaw & Zhang 1992, Zhuang & Amiro 1994), and directly from large eddy simulation (LES) models (Dwyer et al 1997). Our results, like those of Brunet et al (1994), which they

replace, can be reproduced quite well by standard, free-air second-moment parameterizations, and the pattern of  $Tp$  opposing and being slightly smaller than  $Tt$  is the pattern seen in mixing layers (see Figure 11).

Maitani & Seo (1985), in contrast, found the magnitude of  $Tp$  to be about half of  $Tt$  and of the same sign in the lower canopy, while the results of Shaw et al (1990), Shaw & Zhang (1992), and Zhuang & Amiro (1994) all indicate that  $Tp$  is a gain term in the lower canopy. The LES model of Dwyer et al (1997) produced a TKE budget with  $Tp \approx Tt/2$  near  $z = h$ , but  $Tp > Tt$  in the lower canopy, where it was the largest source of TKE. Unfortunately, all four approaches are subject to criticism. First, it is difficult to have much confidence in values of  $Tp$  derived as residuals, especially in the lower canopy where all terms are small. As we have seen, many simplifying assumptions are necessary to calculate the dissipation, while other small terms are simply ignored. Combining surface pressure and measured velocity to form  $\langle \overline{w'p'} \rangle$ , as Maitani & Seo did, ignores the  $z$  dependence of  $p'$ , while experimental constraints have meant that solutions of the Poisson equation tacitly assume that the fluctuation velocity field can be treated as two-dimensional. This assumption is at variance with the strong lateral dependence of the velocity field of a characteristic eddy that we saw in §4.3. LES calculations, while showing great promise, require greater resolution and sub-grid-scale models appropriate to the special character of canopy spectral dynamics before their output can be accepted unequivocally.

At present, therefore, the question of the sign of  $Tp$  in the upper canopy must be viewed as unresolved although it seems very likely that it is a gain in the lower canopy. What is clear is that large transport terms and a balance far from local equilibrium are characteristic features of canopy TKE budgets, and the net transport  $Tt + Tp$  is the main source of TKE in the lower canopy.

Before leaving the TKE budget, we should make two final points. First, the very large total dissipation rate in the canopy means that the eddy timescale  $\tau_e = \langle \overline{u_i' u_i'} \rangle / 2(\varepsilon + W_D)$  drops abruptly as we descend into the canopy. Since  $\varepsilon \ll W_D$  we can use Equation 6.7 to approximate  $\tau_e$  as  $\tau_e = (C_D a \langle \overline{u_1} \rangle)^{-1}$ . Turbulence produced by the efficient inflection-point instability process is rapidly shunted to dissipation scales by interaction with the vegetation. The rate of dissipation adjusts to this large spectral energy flux because the high intensity shear layers that develop around the plant parts are efficient sources of dissipation themselves (Ayotte et al 1999). This potential for rapid adjustment of the within-canopy flow to changing rates of TKE production has obvious implications for non-equilibrium situations.

Second, we must remember that the processes we are parameterizing by the  $W_D$  term are not viscous dissipation itself but the anisotropic interaction of turbulent velocity components with the canopy drag. As such,  $W_D$  affects covariances as well as normal stresses and proves to be a substantial sink term for shear stress within the canopy as it acts to reduce the anisotropy of turbulent velocity components (Ayotte et al 1999).

## 8. CONCLUSIONS AND FUTURE DIRECTIONS

### 8.1 A Summary of Uniform Canopy Flow

Canopy turbulence owes its special character to two interdependent processes: The dynamics, scale, and energetics of the large eddies are determined by an inflection-point instability centered around the top of the vegetation. The inflection-point profile develops because canopies absorb momentum over a space extended in the vertical rather than just at the ground surface, and the scale of the inflected profile is linked to the canopy height and density. The absorption of momentum by aerodynamic drag on the foliage goes hand in hand with a very rapid rate of dissipation of turbulent kinetic energy. The process of dissipation itself is enhanced because the vegetation is an abundant source of intense shear layers of very fine scale. At the same time, the transfer of TKE from the energy-containing scales to dissipation scales is greatly enhanced by the spectral short-cut that occurs as the larger eddies do work against the pressure drag of the foliage and generate eddies of wake scale.

Because it explains so many of the unique properties we observe, this new picture of canopy dynamics has supplanted the earlier view that supposed the roughness sublayer was merely a superposition of plant wakes on the surface layer. To take just one example, the failure of eddy-diffusivity models is not unexpected once we know that the characteristic scale of the dominant eddies is the same as the scale of changes in concentration gradients (Corrsin 1974). From our new viewpoint we know that both are linked to the vertical scale of the foliage distribution or, more simply, just to the canopy height. This picture of canopy dynamics is the result of many careful experiments in the ideal conditions of uniform canopies in steady flows or in wind tunnels. It seems appropriate, therefore, to end this review by making a connection between what we have learned in these simple flows and the untidy clutter of the real world.

### 8.2 Diabatic Effects

We have not discussed the influence of moderate stability and instability on flow dynamics because it is primarily quantitative rather than qualitative. Shaw et al (1988), Gao et al (1989), and Leclerc et al (1990) have used  $h/L$  (where  $L$  is the Obukhov length calculated above  $z = h$ ) to characterize diabatic effects on TKE and Reynolds stress budgets and on large eddy structure, but no universal behavior has yet emerged. In general, canopies are very rough surfaces in an aerodynamic sense, so quite large values of  $|h/L|$  are required before a significant influence of buoyancy is discernable.

It is at times of strong stability that we observe qualitative differences in the flow field. Most solar radiation is absorbed in the upper 30% of closed canopies, and it is this part of the canopy that actively radiates to the cold sky at night. As a result, during the day the lower part of the canopy airspace is often stably

stratified while the upper canopy and the surface layer above is unstable. In the daytime in light winds and strong insolation, weak gravity waves have been observed in the open trunkspace of forests, but it is the stable nighttime situation that offers the most dramatic effects. If the surface layer and upper canopy are stably stratified and the lower canopy unstable, a critical level for diabatically forced Kelvin-Helmholtz instabilities (Richardson number  $< 1/4$ ) is bound to exist near the top of the canopy, and active periods of gravity waves are a characteristic part of nocturnal canopy dynamics (Lee & Barr 1998). Understanding their role in the nighttime exchange of scalars like carbon dioxide is currently an active research question.

### 8.3 Inhomogeneous Canopy Flows

We divide this topic into two categories: In the first category are canopies on hills, with windbreaks and near clearings or edges; in the second are canopies with sparse or non-uniform vegetation. In these two- and three-dimensional situations, it is very difficult to obtain detailed data in the field as multiple towers are required. Hence the most complete information has come from the wind tunnel such as the study of a tall canopy on a hill by Finnigan & Brunet (1995) or of a canopy with multiple windbreaks by Judd et al (1996). Logistical difficulties notwithstanding, useful field studies have been done of flow over forest edges, for example, by Kruijt et al (1995) and Irvine et al (1997).

One of the most interesting thing about these disturbed flows is the way that the interplay between mean pressure gradients, mean flow acceleration, turbulent stress divergence, and aerodynamic drag can alter the inflection-point profile that is central to the mixing layer hypothesis. Finnigan & Brunet (1985) showed that there is a natural length-scale over which a new equilibrium is reached in the canopy momentum balance. This length is  $(C_D a)^{-1}$ , which, not surprisingly, is related to the turbulent relaxation time in the canopy,  $\tau_e = (\langle \overline{u_1} \rangle C_D a)^{-1}$  (§7.0). A quite different balance is struck above the canopy, where aerodynamic drag is absent and large phase differences can appear between the mean velocity within and above the canopy, when a large-scale pressure field is imposed.

Finnigan & Brunet (1995) found that the inflection point in the profile completely disappeared partway up the hill and was strongly exaggerated at the hill crest, where  $L_s$ , the shear length scale, dropped to about one third of its equilibrium value. Similar strong variations in  $L_s$  are observed at a forest edge with  $L_s$  growing with downwind distance until it finds an equilibrium value. Behind windbreaks the canopy-top shear can be completely removed just behind the barrier, taking several multiples of  $(C_D a)^{-1}$  before it is reestablished.

A different set of variations from our ideal picture is found in sparse canopies like orchards, thinned forests, or savannah woodlands. It is evident that at some point the canopy may become sufficiently sparse that a dynamically significant inflection-point profile ceases to exist, and canopy turbulence is simply a super-



position of wakes from isolated plants. It is a question of real interest to know at what point this change-over starts to take place, as it delimits the parameter space within which models meant for uniform canopies may be applied. A recent wind tunnel study by Novak et al (2000) has found departures from the mixing-layer-analogy relationship  $\Lambda_x = 8.1L_s$  (Figure 12) as the canopy roughness index  $\lambda$  (see Table 1) dropped below 1.0.

These difficult inhomogeneous situations demand two- and three-dimensional deployment of instruments to capture their character properly, and for field experiments in tall canopies especially, this is a daunting prospect. One of the most promising recent developments in canopy studies, therefore, is the use of LES models. The pioneering efforts of Shaw & Schumann (1992) have been followed by several other studies that show excellent correspondence with measured field and wind tunnel data. Dwyer et al (1997) illustrated the power of LES models to calculate essentially unobservable terms like  $p'$ , while Su et al (1998) tackled a sparse forest canopy and Patton et al (1998) showed the ability of the technique to deal with truly inhomogeneous situations in their simulation of windbreak flows. There is little doubt that a hallmark of the next two decades of canopy studies will be increasing reliance on such simulations to augment measurement.

#### ACKNOWLEDGMENTS

I would like to thank the several authors who have allowed me to use figures from their papers in this review. I also wish to acknowledge the fruitful interaction I have enjoyed over the years in the field of canopy studies with my friends and colleagues, Dr. EF Bradley, Dr. OT Denmead, Dr. R Leuning, and Dr. Keith Ayotte. I would like to single out for particular mention Dr. MR Raupach, Dr. Y Brunet, and Professor R Shaw, with whose collaboration many of the ideas and theories contained in this review were developed. During the writing of this review the author was on sabbatical leave at NCAR, Boulder, Colorado, and the support of the Mesoscale and Microscale Meteorology Division and the Geophysical Turbulence Program of NCAR is gratefully acknowledged.

**Visit the Annual Reviews home page at [www.AnnualReviews.org](http://www.AnnualReviews.org).**

#### LITERATURE CITED

- |   |   |
|---|---|
| Allen LH. 1968. Turbulence and wind speed spectra within a Japanese larch plantation. <i>J. Appl. Meteorol.</i> 7:73–78                 | Antonia RA. 1981. Conditional sampling in turbulence measurement. <i>Annu. Rev. Fluid Mech.</i> 13:131–56   |
| Amiro BD. 1990. Drag coefficients and turbulence spectra within three boreal forest canopies. <i>Boundary-Layer Meteorol.</i> 52:227–46 | Ayotte KW, Finnigan JJ, Raupach MR. 1999. A second-order closure for neutrally stratified vegetative canopy flows. <i>Boundary-Layer Meteorol.</i> 90:189–216 |

- Baldocchi DD, Meyers TP. 1988a. A spectral and lag-correlation analysis of turbulence in a deciduous forest canopy. *Boundary-Layer Meteorol.* 45:31–58
- Baldocchi DD, Meyers TP. 1988b. Turbulence structure in a deciduous forest. *Boundary-Layer Meteorol.* 43:345–64
- Baldocchi DD, Meyers TP. 1998. On using eco-physiological, micrometeorological and biogeochemical theory to evaluate carbon dioxide, water vapor and gaseous deposition fluxes over vegetation. *Agric. For. Meteorol.* 90:1–26
- Batchelor GK. 1959. *The Theory of Homogeneous Turbulence*. London: Cambridge Univ. Press
- Bergström H, Höglström U. 1989. Turbulent exchange above a pine forest. II. Organized structures. *Boundary-Layer Meteorol.* 49:231–63
- Browand FK, Troutt TR. 1980. A note on spanwise structure in the two-dimensional mixing layer. *J. Fluid Mech.* 97:771–81
- Brown GL, Roshko A. 1974. On density effects and large structure in turbulent mixing layers. *J. Fluid Mech.* 64:775–816
- Brunet Y, Finnigan JJ, Raupach MR. 1994. A wind tunnel study of air flow in waving wheat: single-point velocity statistics. *Boundary-Layer Meteorol.* 70:95–132
- Cantwell BJ. 1981. Organized motion in turbulent flow. *Annu. Rev. Fluid Mech.* 13:437–515
- Collineau S, Brunet Y. 1993. Detection of turbulent coherent motions in a forest canopy, Part II: Timescales and conditional averages. *Boundary-Layer Meteorol.* 66:49–73
- Comte P, Lesieur M, Lamballais E. 1992. Large and small-scale stirring of vorticity and a passive scalar in a 3-D temporal mixing layer. *Phys. Fluids A* 4:2761–78
- Coppin PA, Raupach MR, Legg BJ. 1986. Experiments on scalar dispersion within a model plant canopy. II. An elevated plane source. *Boundary-Layer Meteorol.* 35:167–91
- Corrsin S. 1974. Limitations of gradient transport models in random walks and turbulence. *Adv. Geophys.* 18A:25–60
- Denmead OT, Bradley EF. 1985. Flux-gradient relationships in a forest canopy. In *The Forest-Atmosphere Interaction*, ed. BA Hutchison, BB Hicks, pp. 421–42. Dordrecht, The Netherlands: Reidel
- Denmead OT, Bradley EF. 1987. On scalar transport in plant canopies. *Irrig. Sci.* 8:131–49
- Dimotakis PE, Brown GL. 1976. The mixing layer at high Reynolds number: large structure dynamics and entrainment. *J. Fluid Mech.* 78:535–60
- Drazin PG, Reid WH. 1981. *Hydrodynamic Stability*. Cambridge, UK: Cambridge Univ. Press. 527 pp.
- Dwyer MJ, Patton EG, Shaw RH. 1997. Turbulent kinetic energy budgets from a large-eddy simulation of airflow above and within a forest. *Boundary-Layer Meteorol.* 84:23–43
- Finnigan JJ. 1979. Turbulence in waving wheat II. Structure of momentum transfer. *Boundary-Layer Meteorol.* 16:213–36
- Finnigan JJ. 1985. Turbulent transport in flexible plant canopies. In *The Forest-Atmosphere Interaction*, ed. BA Hutchison, BB Hicks, pp. 443–80. Dordrecht, The Netherlands: Reidel
- Finnigan JJ, Brunet Y. 1995. Turbulent airflow in forests on flat and hilly terrain. In *Wind and Trees*, ed. MP Coutts, J Grace, pp. 3–40. Cambridge, UK: Cambridge Univ. Press
- Finnigan JJ, Raupach MR. 1987. Transfer processes in plant canopies in relation to stomatal characteristics. In *Stomatal Function*, ed. E Zeiger, GD Farquar, IR Cowan, pp. 385–429. Stanford, CA: Stanford Univ. Press. 503 pp.
- Finnigan JJ, Shaw RH. 2000. A wind tunnel study of airflow in waving wheat: an Empirical Orthogonal Function analysis of the large-eddy motion. *Boundary-Layer Meteorol.* In press

- Gao W, Shaw RH, Paw U KT. 1989. Observation of organised structure in turbulent flow within and above a forest canopy. *Boundary-Layer Meteorol.* 47:349–77
- Gardiner BA. 1994. Wind and wind forces in a plantation spruce forest. *Boundary-Layer Meteorol.*, 67:161–86
- Garratt JR. 1992. *The Atmospheric Boundary Layer*. Cambridge, UK: Cambridge Univ. Press. 316 pp.
- Irvine MR, Gardiner BA, Hill MK. 1997. The evolution of turbulence across a forest edge. *Boundary-Layer Meteorol.* 84:467–96
- Judd MJ, Raupach MR, Finnigan JJ. 1996. A wind tunnel study of turbulent flow around single and multiple windbreaks, Part one: Velocity fields. *Boundary-Layer Meteorol.* 80:127–65
- Kaimal JC, Finnigan JJ. 1994. *Atmospheric Boundary Layer Flows: Their Structure and Measurement*. New York: Oxford Univ. Press. 289 pp.
- Kruijt B, Klaassan W, Hutjes RWA. 1995. Adjustment of turbulent momentum flux over forest downwind of an edge. In *Wind and Trees*, ed. MP Coutts, J Grace. Cambridge, UK: Cambridge Univ. Press. 485 pp.
- Leclerc MY, Beissner KC, Shaw RH, Den Hartog G, Neumann HH. 1990. The influence of atmospheric stability on the budgets of the Reynolds stress and turbulent kinetic energy within and above a deciduous forest. *J. Appl. Meteorol.* 29:916–33
- Lee X, Barr AG. 1998. Climatology of gravity waves in a forest. *Q. J. R. Meteorol. Soc.* 124:1403–19
- Lee X, Black TA. 1993. Atmospheric turbulence within and above a Douglas Fir stand. Part II: Eddy fluxes of sensible heat and water vapor. *Boundary-Layer Meteorol.* 64:369–89
- Leonard A. 1974. Energy cascade in large-eddy simulations of turbulent fluid flows. *Adv. Geophys.* 18A:237–48
- Lu SS, Willmarth WW. 1973. Measurements of the structure of Reynolds stress in a turbulent boundary layer. *J. Fluid Mech.* 60:481–571
- Lu CH, Fitzjarrald DR. 1994. Seasonal and diurnal variations of coherent structures over a deciduous forest. *Boundary-Layer Meteorol.* 69:43–69
- Lumley JL. 1964. The spectrum of nearly inertial turbulence in a stably stratified fluid. *J. Atmos. Sci.* 21:99–102
- Lumley JL. 1967. The structure of inhomogeneous turbulent flows. In *Atmospheric Turbulence and Radio Wave Propagation*, ed. AM Yaglom, VI Tatarsky, pp. 166. Moscow: Nauka
- Lumley JL. 1981. Coherent structures in turbulence. In *Transition and Turbulence*, ed. RE Meyer, pp. 215–41. Mathematics Research Center Symposia and Advanced Seminar Series. New York: Academic
- Maitani T, Seo T. 1985. Estimates of velocity-pressure and velocity-pressure-gradient interactions in the surface layer over canopies. *Boundary-Layer Meteorol.* 33:51–60
- Maitani T, Shaw RH. 1990. Joint probability analysis of momentum and heat fluxes at a deciduous forest. *Boundary-Layer Meteorol.* 52:283–300
- Meyers TP, Baldocchi DD. 1991. The budgets of turbulent kinetic energy and Reynolds stress within and above a deciduous forest. *Agric. For. Meteorol.* 53:207–22
- Michalke A. 1964. On the inviscid instability of the hyperbolic-tangent velocity profile. *J. Fluid Mech.* 19:543–56
- Michalke A. 1965. On spatially growing disturbances in an inviscid shear layer. *J. Fluid Mech.* 23:521–44
- Moin P, Moser RD. 1989. Characteristic-eddy decomposition of turbulence in a channel. *J. Fluid Mech.* 200:471–509
- Novak MD, Warland JS, Orchansky AL, Ketler R, Green S. 2000. Comparison between wind tunnel and field measurements of turbulent flow. Part 1: Uniformly thinned forests. *Boundary-Layer Meteorol.* In press
- Pao YH. 1965. Structure of turbulent velocity and scalar fields at large wavenumbers. *Phys. Fluids* 8:1063–75

- Patton EG, Shaw RH, Judd MJ, Raupach MR. 1998. Large-eddy simulation of windbreak flow. *Boundary-Layer Meteorol.* 87:275–306
- Paw U KT, Brunet Y, Collineau S, Shaw RH, Maitani T, et al. 1992. On coherent structures in turbulence above and within agricultural plant canopies. *Agric. For. Meteorol.* 61:55–68. (Corrigendum: *Agric. For. Meteorol.* 63:127)
- Pierrehumbert RT, Widnall SE. 1982. The two and three-dimensional instabilities of a spatially periodic shear layer. *J. Fluid Mech.* 112:467–74
- Raupach MR. 1989. Stand overstorey processes. *Philos. Trans. R. Soc. Lond. B* 324:175–90
- Raupach MR, Antonia RA, Rajagopalan S. 1991. Rough-wall turbulent boundary layers. *Appl. Mech. Rev.* 44:1–25
- Raupach MR, Coppin PA, Legg BJ. 1986. Experiments on scalar dispersion within a model plant canopy. Part I: The turbulence structure. *Boundary-Layer Meteorol.* 35:21–52
- Raupach MR, Finnigan JJ, Brunet Y. 1989. Coherent eddies in vegetation canopies. *Proc. Australasian Conf. Heat Mass Transfer*, 4th, May 9–12, Christchurch, New Zealand, pp. 75–90.
- Raupach MR, Finnigan JJ, Brunet Y. 1996. Coherent eddies and turbulence in vegetation canopies: the mixing layer analogy. *Boundary-Layer Meteorol.* 78:351–82
- Raupach MR, Shaw RH. 1982. Averaging procedures for flow within vegetation canopies. *Boundary-Layer Meteorol.* 22:79–90
- Raupach MR, Thom AS. 1981. Turbulence in and above plant canopies. *Annu. Rev. Fluid Mech.* 13:97–129
- Robinson SK. 1991. Coherent motions in the turbulent boundary layer. *Annu. Rev. Fluid Mech.* 23:601–39
- Rogers MM, Moser RD. 1992. The three-dimensional evolution of a plane mixing layer: the Kelvin-Helmholtz rollup. *J. Fluid Mech.* 243:183–226
- Saddoughi SG, Veeravalli SV. 1994. Local isotropy in turbulent boundary layers at high Reynolds number. *J. Fluid Mech.* 268:333–72
- Seginer I, Mulhearn PJ. 1978. A note on vertical coherence of streamwise turbulence inside and above a model plant canopy. *Boundary-Layer Meteorol.* 14:515–23
- Seginer I, Mulhearn PJ, Bradley EF, Finnigan JJ. 1976. Turbulent flow in a model plant canopy. *Boundary-Layer Meteorol.* 10:423–53
- Shaw RH. 1977. The influence of vegetation on canopy flow. In *Proc. 13<sup>th</sup> Am. Meteorol. Soc. Conf. on Agric. and For. Meteorol.*, pp. 9–10. Purdue Univ., Indiana
- Shaw RH, Brunet Y, Finnigan JJ, Raupach MR. 1995. A wind tunnel study of air flow in waving wheat: two-point velocity statistics. *Boundary-Layer Meteorol.* 76:349–76
- Shaw RH, Den Hartog G, Neumann HH. 1988. Influence of foliar density and thermal stability on profiles of Reynolds stress and turbulent intensity in a deciduous forest. *Boundary-Layer Meteorol.* 45:391–409
- Shaw RH, Paw U KT, Gao W. 1989. Detection of temperature ramps and flow structures at a deciduous forest site. *Agric. For. Meteorol.* 47:123–38
- Shaw RH, Paw U KT, Zhang XJ, Gao W, Den Hartog G, Neumann HH. 1990. Retrieval of turbulent pressure fluctuations at the ground surface beneath a forest. *Boundary-Layer Meteorol.* 50:319–38
- Shaw RH, Schumann U. 1992. Large-eddy simulation of turbulent flow above and within a forest. *Boundary-Layer Meteorol.* 61:47–64
- Shaw RH, Seginer I. 1985. The dissipation of turbulence in plant canopies. Extended abstract: *Am. Meteorol. Soc. 7<sup>th</sup> Symp. on Turbulence and Diffusion Abstracts*, pp 200–3.
- Shaw RH, Silversides RH, Thurtell GW. 1974. Some observations of turbulence and turbulent transport within and above plant canopies. *Boundary-Layer Meteorol.* 5:429–49
- Shaw RH, Tavanger J, Ward DP. 1983. Structure of the Reynolds stress in a canopy layer. *J. Climate Appl. Meteorol.* 22:1922–31

- Shaw RH, Zhang XJ. 1992. Evidence of pressure-forced turbulent flow in a forest. *Boundary-Layer Meteorol.* 58:173–288
- Sreenivasen KR, Narasimha R. 1978. Rapid distortion of axisymmetric turbulence. *J. Fluid Mech.* 84:497–516
- Su H-B, Shaw RH, Paw U KT, Moeng C-H, Sullivan PP. 1998. Turbulent statistics of neutrally stratified flow within and above a sparse forest from large-eddy simulation and field observations. *Boundary-Layer Meteorol.* 88:363–97
- Thom AS. 1968. The exchange of momentum, mass and heat between an artificial leaf and airflow in a wind tunnel. *Q. J. R. Meteorol. Soc.* 94:44–55
- Townsend AA. 1976. *The Structure of Turbulent Shear Flow*. Cambridge, UK: Cambridge Univ. Press. 429 pp.
- Wilson JD. 1988. A second-order closure model for flow through vegetation. *Boundary-Layer Meteorol.* 42:371–91
- Wilson JD, Ward DP, Thurtell GW, Kidd GE. 1982. Statistics of atmospheric turbulence within and above a corn canopy. *Boundary-Layer Meteorol.* 24:495–519
- Wilson NR, Shaw RH. 1977. A higher order closure model for canopy flow. *J. Appl. Meteorol.* 16:1198–1205
- Winant CD, Browand FK. 1974. Vortex pairing: the mechanism of turbulent mixing layer growth at moderate Reynolds number. *J. Fluid Mech.* 63:237–55
- Zhuang Y, Amiro BD. 1994. Pressure fluctuations during coherent motions and their effects on the budgets of turbulent kinetic energy and momentum flux within a forest canopy. *J. Appl. Meteorol.* 33:704–11

